



This is a repository copy of *The architecture of the Gram-positive bacterial cell wall*.

White Rose Research Online URL for this paper:
<http://eprints.whiterose.ac.uk/160585/>

Version: Accepted Version

Article:

Pasquina-Lemonche, L., Burns, J., Turner, R.D. et al. (8 more authors) (2020) The architecture of the Gram-positive bacterial cell wall. *Nature*. ISSN 0028-0836

<https://doi.org/10.1038/s41586-020-2236-6>

This is a post-peer-review, pre-copyedit version of an article published in *Nature*. The final authenticated version is available online at: <http://dx.doi.org/10.1038/s41586-020-2236-6>

Reuse

Items deposited in White Rose Research Online are protected by copyright, with all rights reserved unless indicated otherwise. They may be downloaded and/or printed for private study, or other acts as permitted by national copyright laws. The publisher or other rights holders may allow further reproduction and re-use of the full text version. This is indicated by the licence information on the White Rose Research Online record for the item.

Takedown

If you consider content in White Rose Research Online to be in breach of UK law, please notify us by emailing eprints@whiterose.ac.uk including the URL of the record and the reason for the withdrawal request.



eprints@whiterose.ac.uk
<https://eprints.whiterose.ac.uk/>

The Architecture of the Gram Positive Bacterial Cell Wall

L. Pasquina-Lemonche^{1,2,3†}, J. Burns^{1,2,3†}, R.D. Turner^{1,4,5}, S. Kumar^{1,2,6}, R. Tank^{1,2}, N. Mullin^{1,2}, J.S. Wilson^{1,4}, B. Chakrabarti², P.A. Bullough^{1,4}, S.J. Foster^{1,3,4*}, J.K. Hobbs^{1,2,3*}

† These authors contributed equally to this work

¹ Krebs Institute, University of Sheffield. S10 2TN. UK

² Dept. Physics and Astronomy, University of Sheffield. S3 7RH. UK

³ The Florey Institute, University of Sheffield. S10 2TN. UK

⁴ Dept. Molecular Biology and Biotechnology, University of Sheffield. S10 2TN. UK

⁵ Current address: Department of Computer Science, University of Sheffield. S1 4DP. UK

⁶ Current address: Dept. of Biochemistry, University of Oxford. OX1 3QU

* For further information contact s.foster@sheffield.ac.uk or jamie.hobbs@sheffield.ac.uk

Introduction

The primary structural component of the bacterial cell wall is peptidoglycan, which is essential for viability and whose synthesis is the target for crucial antibiotics^{1,2}. Peptidoglycan is a single macromolecule made of glycan chains crosslinked by peptide side branches that surrounds the cell, acting as a constraint to internal turgor^{1,3}. In Gram positive bacteria peptidoglycan is tens of nanometres thick, generally portrayed as a homogeneous structure providing mechanical strength⁴⁻⁶. Here we applied Atomic Force Microscopy (AFM)⁷⁻¹² to interrogate the morphologically distinct *Staphylococcus aureus* and *Bacillus subtilis* species, using live cells and purified peptidoglycan. The mature surface of live cells is characterised by a landscape of large (up to 60 nm diameter), deep (up to 23 nm) pores constituting a disordered gel of peptidoglycan. The inner peptidoglycan surface, reflecting more nascent material, is much denser with glycan strand spacing typically less than 7 nm. Inner surface architecture is location dependent; the cylinder of *B. subtilis* has dense circumferential orientation, whilst in *S. aureus* and division septa for both species, peptidoglycan is dense but randomly oriented. Revealing the cell envelope molecular architecture frames understanding of its mechanical properties and role as the environmental interface¹³⁻¹⁴, providing information complementary to traditional structural biology approaches.

Exponentially grown *S. aureus* cells were immobilised in microfabricated wells¹⁵ on silicon substrates, and imaged live using small cantilever, small amplitude AFM. Large scans recapitulated known mesh (mature) and ring (freshly revealed division plane) surface architectures of *S. aureus*^{7,8} (Fig 1a). High resolution revealed the mesh (Fig 1b and Extended data ED1) to be randomly oriented strands of varying widths with pores up to 23 nm deep (Fig 1c). As the wall thickness² is approximately 20 nm, some pores must span the majority of, if not the entire, wall. Lack of the major wall-associated polymers, wall teichoic acid (WTA)¹⁶, or lipoteichoic acid (LTA)¹⁷, did not materially alter architecture (ED1), consistent with the observed features being peptidoglycan. Individual strands (Fig 1b) have variable width (mean 6.0 ± 3.8 nm, $n = 45$, Fig 1g) and in some instances (e.g. green dotted arrows, Fig 1b) several individual strands coming together are resolved, so we conclude these fibres are often multi-molecular (e.g. blue arrows, 1b). The peptidoglycan areal density is surprisingly low in the outer wall, typically only 50% is filled at 11 ± 3.4 nm depth, $n = 5$ (Fig 1c, green area). The mature wall outer zone is therefore a porous gel i.e. a 3-dimensional solid mesh in a liquid medium.

The surface ring architecture (attributable to nascent septal material⁷) is initially molecularly dense (Fig 1d,e), composed of radially corrugated groups of circumferentially oriented individual strands, spaced by 2.7 ± 0.5 nm ($n = 16$), (Fig 1f), in the densest regions. Periodic features (spacing 3.7 ± 0.8 nm, $n = 24$) are sometimes observed along the strands (ED1) in agreement with the predicted helical pitch of peptidoglycan¹⁸. The observation of long glycan strands in nascent ring material supports the role of peptidoglycan hydrolases in cell growth associated wall maturation¹⁹. The interface between disordered mesh and ordered rings is sharp (ED2). Cell division occurs in consecutive orthogonal planes, so, as a ring architecture lying orthogonal to rings from a previous generation is not seen, rings transition to mesh within a single division cycle under these growth conditions.

Live cell imaging is limited to the outer surface and does not distinguish constituents. Previous work has shown that imaging extracted, purified, cell wall peptidoglycan (sacculi) in air can provide useful insights into the cell wall architecture through the cell cycle⁷. Here sacculi were imaged in liquid, using PeakForce Tapping, following immobilisation (see Methods). Sacculus fragments exhibit the live cell ring and mesh (previously interpreted as “knobbles”⁷, ED4) architectures (Fig 2a-d). Importantly, within individual sacculi, both internal and external surfaces are observed with AFM (e.g. Fig 2a). Every inner surface image obtained ($n = 80$) exhibited a tight, disordered mesh (Fig 2e,f), made of likely single chains (width 2.8 ± 0.8 nm, $n = 45$, Fig 2j) with diameters of pores covering half of the total pore area being smaller than 6.4 nm ($n = 158$), substantially smaller than the pores on the external surface of live cells (39 nm, $n = 310$) (Fig 2i, ED5, see Methods). Rings are not present on the cytoplasm facing

surface of incomplete septa (Fig 2g-h), which instead have a tight disordered mesh akin to the rest of the internal surface ($n = 25$); for different stages of formation see ED4. The ring architecture is confined to the last generation, post division, septal outer surface. Maturation from rings to mesh likely occurs by loss and re-organisation of surface rings revealing underlying disordered mesh (ED2). The final architecture of the wall is determined by interplay between the cell wall synthesis and hydrolysis enzymes. Removal of one of the peptidoglycan synthesis enzymes, PBP4, results in a denser ring structure, occasionally persisting beyond the first generation surface (ED3). The transition from rings to porous mesh is primarily due to the action of the peptidoglycan hydrolases. Removal of the important enzyme SagB¹⁹ results in initially thinner cell walls that take longer to transition to the mature disordered mesh architecture (ED3).

Electron cryotomography^{5,20} of frozen hydrated *S. aureus* sacculi show both rough and smooth external surfaces (ED6, SI1). When directly compared, the AFM and cryoEM data are complementary and demonstrate the different capabilities of the approaches (ED6k-n). In parts of the external surface of the sacculus cryoEM tomogram, we can see pores in the wall with similar dimensions to those observed with the AFM (ED6e), albeit slightly shallower (most likely due to the resolution of the tomogram), and considerably less distinct (because of the relatively poor contrast that we would expect with cryoEM); compare ED6m/n. In other regions (e.g. bottom right of ED6a) both the inside and outside are quite smooth, with the occasional pore (ED6k). CryoEM is unable to discern the ring structure as it views in transverse section, but we suggest such smooth regions are likely “rings”. Thus, distinct imaging modalities yield corroborative architectural information.

To explore the generality of our observations, the rod-shaped *B. subtilis* was investigated. Exponentially grown live cells were immobilised and imaged on Cell-Tak coated mica. The cell cylinder exhibited a disordered mesh with strands of variable thickness (4.5 ± 1.9 nm, $n = 111$, Fig 3a,b,d), similar to *S. aureus* and contrary to previously proposed circumferentially oriented features⁵. Sequential longitudinal imaging of an individual bacterium revealed no change in architecture away from the poles (ED7). Pores up to 15 nm deep are observed along the cell cylinder (Fig 3c and ED5). *B. subtilis* live-cell poles are challenging to image with AFM due to their orientation relative to the probe tip, however the cylinder-pole interface reveals a pole-associated ring architecture (Fig 3e,f).

Imaging of purified *B. subtilis* sacculi revealed the outer surfaces of the cylinder as randomly oriented mesh (Fig 3g), and the pole as rings (Fig 3h) and mesh (ED7). Contrastingly, the sacculus cylinder inner surface exhibited features that would be oriented approximately around the circumference in vivo (Fig 3i and ED7), at length scales from apparent single

glycans to larger structures, previously interpreted as “cables” in samples imaged in air²¹ and possibly responsible for the contrast described as “circumferentially oriented features” in CryoEM⁵. The internal orientation of the individual strands is circumferential around the cell, in contrast to the helical organisation we previously suggested²¹. Removing the MreB cell shape-determining protein family produced spherical cells with randomly oriented strands, implying that these components are responsible for this circumferential orientation (ED8, SI2)²²⁻²⁴. The cytoplasm facing side of the incomplete septal wall of *B. subtilis* has a disordered mesh architecture (Fig 3j,k), with randomly oriented strands. It also has prominent pores across its surface (ED7,9). The internal surface of the mature poles shows a disordered, relatively dense architecture (ED7) suggesting that the pores in incomplete septa are most likely back-filled independent of leading edge septal synthesis. The more complex septal architecture previously observed²¹ on dried samples probably comes from the interplay between the constraints imposed by “external” rings and “internal” mesh during dehydration (see ED9).

Purified mature sacculi (Peptidoglycan+WTA) of *S. aureus* and *B. subtilis* are respectively 36 ± 5.3 nm ($n = 25$) and 34 ± 10 nm ($n = 19$) in thickness when hydrated and 17 ± 2 nm ($n = 25$) and 9 ± 1 nm thick ($n = 19$) when dried (Fig 2k,l, ED4,9). Previous CryoEM^{4,5} shows a ~50% increase in wall thickness from live cells to extracted, hydrated sacculi. Even on the cytoplasmic facing surface of the wall, the peptidoglycan has a relatively porous structure unlike conventional representation as a dense wall¹⁸. This raises a question of how it fulfils its role containing bacterial turgor pressure. For turgor to cause lysis the membrane must bulge out through the wall, overcoming the bending modulus of the membrane. A calculation of elastic deformation energy (SI3) implies that a pore with diameter of 8 nm could support an internal turgor pressure of ~ 20 bar, i.e. the pores we observe are small enough to support the expected internal pressure on the cell membrane^{25,26}.

The data and interpretation presented here, obtained from live cells and from sacculi imaged in liquid show significant differences from the data taken in air on dried sacculi in our previous studies^{7,21}. Live cell images demonstrate that the mature cell wall is a porous, mesh-like hydrogel (Fig 1b). Images of sacculi in liquid show similar features to the live cell data (Fig 2b), and that there is a large increase in thickness compared to dried sacculi due to swelling upon hydration (Fig 2k,l). We believe the striking differences between our current and previous studies^{7,21} reflect the collapsed nature of the dried sacculi compared to the inherently 3-dimensional nature of the hydrated Gram positive cell wall. This new understanding of cell wall architecture (ED10 shows a schematic representation) sets constraints for those components required for cellular peptidoglycan dynamics. Analysis of two morphologically diverse bacteria reveals a level of commonality not previously observed.

Nascent septa have two distinct peptidoglycan architectures indicating different synthesis regimes. The septum has an external highly ordered structure of approximately concentric rings, which we hypothesise are deposited at the leading edge of the constricting cell membrane^{27,28} forming the post synthesis core, to be revealed during cell separation. Behind this leading edge and responsible for the majority of the septum thickness, is randomly oriented material. This is consistent with bulk peptidoglycan synthesis across the growing septal plate, not limited to the leading edge²⁹. The internal surface of the rest of *S. aureus* is smooth but randomly oriented, with pores small enough to prevent membrane destabilization and subsequent plasmolysis due to internal turgor. *B. subtilis* is similar, apart from a circumferential orientation of material in the cylinder, likely driven by elongasome-associated peptidoglycan synthesis²²⁻²⁴. The external cell surface of both organisms has an architecture formed by the combination of peptidoglycan metabolism and stress due to turgor. Peptidoglycan maturation results in reorientation from septal rings (in *S. aureus*) and circumferential cylinder (in *B. subtilis*) to produce a porous surface architecture.

The cell wall is responsible for roles that have conflicting design requirements. The wall must support the membrane to maintain turgor and prevent lysis, requiring structural rigidity and precluding channels which the plasma membrane could push through. However, the cell requires access to molecules from its environment which need to pass through the wall. The external facing relatively open structure with strands that are multiple molecules thick and hence have relatively high load bearing potential allows ingress of material. However, such large pores are not compatible with preventing membrane escape. The inner wall, with its smaller pore size, but thinner strands (largely single glycan chains) prevents membrane deformation at the point where this is required, i.e. where the wall interfaces with the plasma membrane. Finally, we note that a surface with such a high specific area is ideal for maximising the possible locations for displaying surface proteins and other surface structures.

References

1. Turner, R. D. Vollmer, W. & Foster, S. J. Different walls for rods and balls: The diversity of peptidoglycan. *Mol. Microbiol.* **91**, 862-874 (2014).
2. Vollmer, W. & Seligman, S. J. Architecture of peptidoglycan: more data and more models. *Trends Microbiol.* **18**, 59–66 (2010).
3. Rojas, E. R. et al. The outer membrane is an essential load-bearing element in Gram-negative bacteria. *Nature.* **559**, 617-621 (2018).

4. Matias, V. R. F. & Beveridge, T. J. Native cell wall organization shown by cryo-electron microscopy confirms the existence of a periplasmic space in *Staphylococcus aureus*. *J. Bacteriol.* **183**, 1011-1021 (2006).
5. Beeby, M., Gumbart, J. C., Roux, B. & Jensen, G. J. Architecture and assembly of the Gram-positive cell wall. *Mol. Microbiol.* **88**, 664-672 (2013).
6. Misra, G. et al. Mechanical consequences of cell-wall turnover in the elongation of a gram-positive bacterium. *Biophys. J.* **104**, 2342-2352 (2013).
7. Turner, R. D. et al. Peptidoglycan architecture can specify division planes in *Staphylococcus aureus*. *Nat. Commun.* **1**, 26 (2010).
8. Touhami, A., Jericho, M. H. & Beveridge, T. J. Atomic force microscopy of cell growth and division in *Staphylococcus aureus*. *J. Bacteriol.* **186**, 3286-3295 (2004).
9. Saar Dover, R., Bitler, A., Shimoni, E., Trieu-Cuot, P. & Shai, Y. Multiparametric AFM reveals turgor-responsive net-like peptidoglycan architecture in live streptococci. *Nat. Commun.* **6**, 7193 (2015).
10. Andre, G. et al. Imaging the nanoscale organization of peptidoglycan in living *Lactococcus lactis* cells. *Nat. Commun.* **1**, 27 (2010).
11. Turner, R. D., Mesnage, S., Hobbs, J. K. & Foster, S. J. Molecular imaging of glycan chains couples cell-wall polysaccharide architecture to bacterial cell morphology. *Nat. Commun.* **9**, 1263 (2018).
12. Eskandarian, H. A. et al. Division site selection linked to inherited cell surface wave troughs in mycobacteria. *Nat. Microbiol.* **2**, 17094 (2017).
13. Zhou, X. et al. Mechanical crack propagation drives millisecond daughter cell separation in *Staphylococcus aureus*. *Science.* **348**, 574-578 (2015).
14. Green, E. R. & Mecsas, J. Bacterial Secretion Systems: An Overview. in *Virulence Mechanisms of Bacterial Pathogens*, Fifth Edition (2016).
15. Bailey, R. G. et al. The interplay between cell wall mechanical properties and the cell cycle in *Staphylococcus aureus*. *Biophys. J.* **107**, 2538-2545 (2014).
16. Weidenmaier, C. et al. Role of teichoic acids in *Staphylococcus aureus* nasal colonization, a major risk factor in nosocomial infections. *Nat. Med.* **10**, 243-245 (2004).
17. Matias, V. R. F. & Beveridge, T. J. Lipoteichoic acid is a major component of the *Bacillus*

- subtilis periplasm. *J. Bacteriol.* **190**, 7414-7418 (2008).
18. Kim, S. J., Chang, J. & Singh, M. Peptidoglycan architecture of Gram-positive bacteria by solid-state NMR. *Biochim Biophys Acta.* **1848**, 350-362 (2015).
 19. Wheeler, R. et al. Bacterial cell enlargement requires control of cell wall stiffness mediated by peptidoglycan hydrolases. *MBio.* **6**, 4 (2015).
 20. Gan, L., Chen, S. & Jensen, G. J. Molecular organization of Gram-negative peptidoglycan. *Proc. Natl. Acad. Sci.* **105**, 18953-18957 (2008).
 21. Hayhurst, E. J., Kailas, L., Hobbs, J. K. & Foster, S. J. Cell wall peptidoglycan architecture in *Bacillus subtilis*. *Proc. Natl. Acad. Sci.* **105**, 14603-14608 (2008).
 22. Domínguez-Escobar, J. et al. Processive movement of MreB-associated cell wall biosynthetic complexes in bacteria. *Science.* **333**, 225-228 (2011).
 23. Garner, E. C. et al. Coupled, circumferential motions of the cell wall synthesis machinery and MreB filaments in *B. subtilis*. *Science.* **333**, 222-225 (2011).
 24. Dion, M. F. et al. *Bacillus subtilis* cell diameter is determined by the opposing actions of two distinct cell wall synthetic systems. *Nat. Microbiol.* **4**, 1294-1305 (2019)
 25. Autolytic release and osmotic properties of protoplasts from *Staphylococcus aureus*. *J. Gen. Microbiol.* **16**, 184-194 (1957).
 26. Daly, K. E., Huang, K. C., Wingreen, N. S. & Mukhopadhyay, R. Mechanics of membrane bulging during cell-wall disruption in Gram-negative bacteria. *Phys. Rev. E. Stat. Nonlin, Soft Matter Phys.* **84**, 041922,1-041922,4 (2011).
 27. Bisson-Filho, A. W. et al. Treadmilling by FtsZ filaments drives peptidoglycan synthesis and bacterial cell division. *Science.* **355**, 739-743 (2017).
 28. Monteiro, J. M. et al. Peptidoglycan synthesis drives an FtsZ-treadmilling-independent step of cytokinesis. *Nature.* **554**, 528-532 (2018).
 29. Lund, V. A. et al. Molecular coordination of *Staphylococcus aureus* cell division. *Elife.* **7**, e32057 (2018).

Figure 1 – AFM images of peptidoglycan in living *S. aureus*. **a**, Entire cell, high-pass filtered (filter size = 0.25 μm , horizontal), blue arrow head: mesh, white arrow: rings. Inset (I): Unfiltered image of the same area. Topographic height data scale (DS) = 902 nm. **b**, Image of the external surface of mature *S. aureus* cell wall showing a porous gel structure, white arrow head indicates a feature consistent with a single glycan chain, green dotted arrows examples of strand convergence, and blue arrows multi-strand fibres. DS = 29 nm. **c**, Depth analysis of pores including the area of image **b** (colour scale: Grey 0 nm, Blue = 5 nm, Green = 10 nm, Orange = 15 nm, Purple = 20 nm, White = 23 nm). Profile shows a section through the image at the black dotted line on **c**, coloured lines indicate depths as above, black area shows outline of pores. **d**, Ring architecture. DS = 22 nm. Inset (I): raw data. DS = 476 nm. **e**, Dense rings, white arrows indicating examples of likely individual chains. DS = 23 nm. **f**, Cross-section showing spacing between strands from boxed area in **e**. **g**, Histogram of strand width, full width at half maximum (FWHM) from image **b**, $n = 60$ strands, dotted line shows mean value. Images **b**, **d** and **e** have been plane-fitted to remove cell curvature. For sample size and data reproducibility, see Methods.

Figure 2 – *S. aureus* sacculus architecture. **a**, 3D image of entire sacculus with external (white arrow) and internal (black arrow) surfaces, black dotted area see (ED4). 3D details: see Methods. Data scale (DS) = 205 nm. **b**, Sacculus external mature cell wall from within **a**. DS = 29 nm. **c**, Sacculus fragment with external surface facing upwards. White arrow: mesh, black arrow: rings. DS = 80 nm. **d**, Rings structure. Dotted line: location of profile (inset) showing the width of a likely single glycan. DS = 12 nm. **e**, Sacculus fragment internal surface upwards. White arrow: early septal growth. DS = 330 nm. **f**, Internal sacculus structure from within **e**. DS = 13 nm. **g**, Partially-formed septum, cytoplasmic facing surface upwards. DS = 389 nm. **h**, Inner surface of partially-formed septum (ED4). Inset: orientation diagram (-90 to 90) from MATLAB analysis (ED8). DS = 12 nm. **i**, Graph showing area of each pore vs the cumulative fraction of the total pore area of all pores. Red stars show 50% of cumulative area, i.e. half the total hole area consists of holes smaller/larger than this value. $n = 601$ pores, from 10 images (histograms in ED5). **j**, Histogram of strand width, measured at FWHM from image **f**, $n = 45$ strands. Red dotted line indicates the mean. **k**, Thickness in liquid and air before (left, $n = 25$ sacculi) and after (right, $n = 10$ sacculi) removal of wall teichoic acids, using a paired, two-tailed t test: $p = 2.4 \cdot 10^{-15}$ (left) and $p = 8.3 \cdot 10^{-6}$ (right), boxes represent 25-75% percentile with centre-line Median, black stars show Mean and bars minimum/maximum. **l**, Images of the same sacculus fragment in air (left) and liquid (right) with same DS = 50 nm. See ED4. For sample size and data reproducibility, see Methods.

Figure 3 – AFM images of peptidoglycan of living *B. subtilis* and extracted sacculi. **a**, Cells immediately post-division, division site (green arrow). Data scale (DS) = 324 nm. **b**, Topographic image of mature *B. subtilis* cell wall from within **e**. White arrow a likely single glycan chain. DS = 22 nm. **c**, Depth analysis of pores from image **ED7d** (colour scale: Blue = 5 nm, Green = 10 nm, Orange = 15 nm). Profile taken at the black dotted line on **c**, coloured lines indicate depths as above. DS = 23 nm. **d**, Histogram of strand width, measured at FWHM from image **c** and a similar image, $n = 111$ strands, dotted line shows the mean. **e**, 3D image of pole showing concentric rings: blue arrows show orientation of rings; black arrow indicates mature mesh. 3D details: see Methods. DS = 760 nm. **f**, Image of the interface between disordered mesh and rings from within **e**. Blue arrows: same location as in **e**. DS = 52 nm. **g**, Mature sacculus, DS = 29 nm. **h**, Cell pole. DS = 18 nm. **i**, Internal surface of sacculus from cylinder region. Strands orientated vertically along the short axis of the cell (arrow). DS = 22 nm. **j**, Partially-formed septum flat on the surface. DS = 223 nm. **k**, Cytoplasmic facing side of a partially-formed septum from within inset. DS = 30 nm. Inset: partially-formed septum. DS = 157 nm. For sample size and data reproducibility, see Methods.

Methods

Bacterial Strains and Growth Conditions

S. aureus SH1000 was grown using Tryptone Soya Broth (TSB, 30g/L) / Tryptone Soya Agar (TSA, 15g/L) and *B. subtilis* 168 HR³⁰ was grown using Nutrient Broth (NB) / Nutrient Agar (NA). Cells were taken from an agar plate, placed in the appropriate growth media and then grown at 37°C for 16 hours while being shaken at 250 rpm. These stationary phase cells were then re-suspended in fresh growth media to $OD_{600} = 0.05$, and grown to exponential phase $OD_{600} = 0.3-0.6$. Samples (1 ml) of the cells were then washed once by centrifugation in the imaging buffer. *S. aureus* *ltaS*, *tarO*, *sagB*, *pbp3* and *pbp4* mutated cells were constructed in the SH1000 background. *B. subtilis* *mreB* *mbl* *mreBH* mutated cells were constructed in an *rsgL* background strain³⁵.

Purification of Peptidoglycan Sacculi

Peptidoglycan was purified as described previously^{7,21,32}. Briefly, bacteria were grown to exponential phase then broken and treated with SDS to solubilise and wash off cellular constituents not covalently bound to peptidoglycan. The resulting material was then treated with pronase to remove covalently bound proteins, and hydrofluoric acid to remove teichoic acids (images Fig 2c,k, Fig 3g-k and all images of sacculi in the ED except where stated omit the final HF treatment). These steps ensure that only peptidoglycan is present in the sacculi,

and can be imaged directly. These processes (apart from cell breaking which has a localised effect) do not affect covalent bonds within the peptidoglycan which are primarily responsible for peptidoglycan structure. However, any stretching or compression of the material *in vivo* by turgor is eliminated in its absence and this must be considered when interpreting data.

Preparation of Silicon Substrates

Silicon substrates were prepared as previously described^{15,33}. Briefly silicon wafers were patterned using photolithography and dry etching to form holes in which spherical bacteria could be immobilised. Additional silicon grids of 1 μm diameter holes were custom made by NuNano (Bristol, UK) and were used to produce images ED1 e-h.

Preparation of Cell-Tak Coated Substrates

Cell-Tak glass slides were prepared by pipetting 285 ml 100 mM NaHCO_3 (pH 8) onto high precision cover glass (24x24 mm^2) then 10 μl of Cell-Tak (Corning, 5% (w/v) in acetic acid) and 5 μl of 1 M NaOH. This was covered and left for 20 minutes. The slide was then washed five times with HPLC grade water. The same process with proportionately smaller volumes was used for coating freshly cleaved mica.

Preparation of Poly-L-Lysine Coated Substrates

Glass coverslips or freshly cleaved mica discs were coated with 0.1% (w/v) in H_2O poly-L-lysine by pipetting on 50 μl and incubating for 20 minutes. The substrate was then washed five times with HPLC grade water and dried with flowing nitrogen.

Immobilising Live *S. aureus* for AFM Imaging

10 μl of bacteria suspension was added to a silicon substrate (see above), left for 30 minutes then the liquid evaporated with nitrogen. Just before all of the liquid was evaporated additional imaging buffer was added. To obtain images ED1 e-h 50 μl of bacteria suspension was added to the NuNano silicon grids and spun down for 3 min at no more than 1500 rpm, then left for 30 min and dried with nitrogen. The sample was rinsed with pure water and imaging buffer added.

Immobilising Live *B. subtilis* for AFM Imaging

A drop of bacteria suspension was added to a Cell-Tak coated substrate. This was then incubated for 30 minutes before five washes in imaging buffer.

Immobilising Sacculi for AFM Imaging

Sacculi stocks were briefly tip-sonicated to re-suspend, then centrifuged for 30 s at 1205 x g to remove large aggregates before being diluted at ~5% volume with 10 mM Tris (pH 8) or further HPLC grade water (choice of solution did not affect image quality). The resulting suspension was incubated for 10-30 minutes (optimal time was determined empirically for each batch of sample, using 10 μ l of sacculi dilution) on either a Cell-Tak or poly-L-lysine coated substrate. In some instances, the sacculi were then dried onto the substrate with flowing nitrogen and rehydrated again for imaging. Similar images were obtained both with and without drying implying minimal disruption of the sacculi from the drying process. Samples were finally washed 3 times with 10 mM Tris (pH 8) before imaging buffer was applied.

AFM Probes

FastScan-D probes (Bruker), nominal spring constant 0.25 N m⁻¹, resonant frequency (in liquid) 110 kHz were used for all presented images taken in liquid. Tespa-V2 probes (Bruker), nominal spring constant of 37 N m⁻¹, resonant frequency (in air) 320 kHz, were used for all experiments in air.

AFM Imaging (Liquid - JPK)

Imaging was carried out in “QI” mode driven at ~167 Hz with a typical Z length of ~ 300 nm using peak interaction forces of 2-3 nN. Images were processed with Gwyddion³⁴.

AFM Imaging (Liquid - Dimension FastScan Bio)

Unless otherwise stated data were collected on this instrument. Live cell imaging was carried out in “Tapping Mode” under a buffer comprised of 300 mM KCl, 10 mM Tris, pH 7.8 using Bruker FastScanD probes driven at ~80 kHz with a typical free amplitude of ~1-2 nm and a set-point amplitude typically ~60-90% of the free amplitude³⁵. This corresponds to average tip-sample forces ~ 100 pN. Imaging of the external surface of sacculi at high resolution with “Tapping Mode” was not achieved, possibly because of the diffuse nature of the surface when relaxed. Sacculi imaging was instead carried out in “PeakForce Tapping” mode³⁶ with a typical amplitude of 100-200 nm, frequency of 2-8 kHz and setpoint force of 1-2 nN with buffer conditions which varied across the samples between HPLC water and 150-300 mM KCl +10mM Tris (pH 8). All images are topographic images unless otherwise stated. All 3D visuals were created using Nanoscope Analysis software.

AFM Imaging (Air - Dimension FastScan Bio)

Unless otherwise stated images were taken under liquid. For some experiments, imaging in air was required. The images were carried out in “Tapping Mode” in air using TESPA-V2,

resonant frequency ~300 kHz, typical imaging free amplitude of ~10-13 nm, set-point amplitude typically ~50-70% of the free amplitude. This corresponds to time averaged tip-sample forces of 260-450 pN.

AFM image 3D details

Fig 2a z aspect ratio = 1, Pitch = 17°, Plot type = height. **Fig 3e** z aspect ratio = 1, Pitch = 33°, Light Pitch 72°, Light Intensity = 55%, Plot type = mixed – colour scale mixes topography and lighting.

Electron cryotomography

A volume of 3.5 µl from HF treated *S. aureus* sacculi mixed with BSA treated 10 nm gold was applied to Lacey carbon grids twice and double blotted before plunge freezing in liquid ethane using a Leica EM GP2 plunge freezer. Tomograms were collected on a FEI Tecnai Arctica microscope operated at 200 kV, with a Falcon III direct electron detector and Volta phase plate. Each tomogram was collected at a nominal defocus of 3 µm, with a total dose applied to the sample of 120 e/Å over ±60° in 2° increments, with a nominal pixel size of 4.3 Å. Tomograms were reconstructed with IMOD³⁷, using weighted back projection and a final binning of 3. Tomograms were filtered with nonlinear anisotropic diffusion (NAD) in order to improve contrast.

Statistical Analyses and Reproducibility

For measurements performed on AFM images of strand widths (represented in histograms in Fig 1g, Fig 2h and Fig 3b), three manual profiles were made for each individual strand using full width at half maximum (FWHM) and then averaged. The mean value and standard deviation (s.d.) was calculated from the total number of fibres 'n'. For fibre spacing and repetitive structures only one profile was taken for each feature and the distance peak-to-peak was measured (e.g. Fig 1g and ED 1), then the mean and standard deviation was calculated from n = 16 and n = 24 respectively. Throughout the text all numbers are presented as <value> ± <s.d.> <unit>.

The thickness of sacculi was measured from histograms of height images. Mean and standard deviation values were calculated from each group (air or liquid). To compare data between groups, paired t tests were performed: with t = 17, degree of freedom (DF) = 24 and p = 2.4×10⁻¹⁵ for peptidoglycan+WTA (Fig 2k, left); t = 9, DF = 9 and p = 8.3×10⁻⁶ for peptidoglycan (Fig 2k, right), t = 11, DF = 18 and p = 1.2×10⁻⁹ for *B. subtilis* sacculi ED9.

For measurements of pore area (diameter), the value given in the text (6.8 nm for internal and 38.4 nm for the external) was extracted from the point where the cumulative fraction of total

pore area (sum of all data) was 0.5, for each distribution. It was not possible to obtain a standard deviation because both distributions are non-normal and positively skewed. The distribution for pores on the external surface can be characterized with the following parameters: $Q_1(25\%) = 4.1$ nm; $Q_2(50\%) = 8.4$ nm; $Q_3(75\%) = 17.4$ nm; $Q_4(90\%) = 33.8$; with $n = 310$ individual pores measured and a mode of $2.5 \leq 3.5 \leq 4.4$ nm. The distribution on the internal surface was characterized as the following: $Q_1(25\%) = 2.5$ nm; $Q_2(50\%) = 3.5$ nm; $Q_3(75\%) = 5.3$ nm; $Q_4(90\%) = 6.1$; with $n = 112$ individual pores and a mode of $1.8 \leq 2.5 \leq 3.1$ nm (see ED5 to visualize histograms and analysis method³⁸).

All statistical analyses were performed with GraphPad Prism 7.04.

Each AFM image or pair of images from living cells in Figure 1 and 3 was performed on freshly cultured cells with a total of $n = 4$ and 3 biological replicates respectively. The two different external morphologies of PG on cells were also detected in at least 5 other biological independent repeats for both *S. aureus* and *B. subtilis* (see repository). The sacculi images from Figure 2 and 3 were obtained from different stocks (see Reporting Summary) as a total of $n = 3$ and 2 biological replicates respectively. The different morphologies of sacculi were detected in at least 5 other technical independent repeats for *S. aureus* and *B. subtilis* (see ED7-9 and repository).

Method references

30. De Jong, I.G., Beilharz, K., Kuipers, O. & Veening, J.W. Live cell imaging of *Bacillus subtilis* and *Streptococcus pneumoniae* using automated time-lapse microscopy. *J. Vis. Exp.* **53**, e3145 (2011).
31. Schirner, K. & Errington, J. The cell wall regulator σ^l specifically suppresses the lethal phenotype of *mbl* mutants in *Bacillus subtilis*. *J. Bacteriol.* **191**, 1404-1413 (2009).
32. Turner, R.D., Foster, S.J., Hobbs, J.K. "Atomic force microscopy analysis of bacterial cell wall peptidoglycan architecture" In: Hong HJ, ed. *Bacterial Cell Wall Homeostasis: Methods and Protocols*. Springer New York, 3-9 (2016)
33. Kailas, L. et al. Immobilizing live bacteria for AFM imaging of cellular processes. *Ultramicroscopy.* **109**, 775-780 (2009).
34. D. Nečas & P. Klapetek. Gwyddion: An open-source software for SPM data analysis. *Cent. Eur. J. Phys.* **10**, 181–188 (2012).
35. Kumar, S. et al. Direct Imaging of Protein Organization in an Intact Bacterial Organelle Using High-Resolution Atomic Force Microscopy. *ACS Nano.* **11**, 126-133 (2017).

36. Su, C. Mapping Quantitative Mechanical Properties at Molecular Scale Using Peak Force Tapping AFM. *Microsc. Microanal.* **16**, 364-365 (2010).
37. Kremer JR, Mastronarde DN, McIntosh JR. Computer visualization of three-dimensional image data using IMOD. *J Structl Biol.* **116**, 71–76 (1996).
38. J. Schindelin et al. Fiji: an open-source platform for biological-image analysis. *Nat. Methods.* **9**, 676-682 (2012).

Acknowledgements

This work was funded by the BBSRC (Grant no. BB/L006162/1), the EPSRC (Grant no. EP/M027430/1, EP/J500124/1), The Wellcome Trust (Grant no. 212197/Z/19/Z), the MRC (MR/N002679/1) and UKRI Strategic Priorities Fund (Grant no. EP/T002778/1). JB would like to thank The White Rose University Consortium for his studentship. LPL would like to thank The Florey Institute for her studentship. We acknowledge Jeff Errington and Angelika Grundling for provision of bacterial strains. We acknowledge Joshua Sutton for preparation of pbp3 and pbp4 sacculi samples. Electron microscopy was performed in the CryoEM Facility of the University of Sheffield.

Author information

Contributions

LPL, JB and RDT designed the study, performed the experiments (LPL Fig 2,3, and ED1-5,7-10, JB Fig 1,3 and ED1,2,7, RDT Fig 3 and ED 7,8,10), analysed and interpreted the data, and wrote the manuscript. SK, JSW and RT performed experiments (SK ED1,7,9, JSW ED 6, RT ED 7) analysed and interpreted the data. NM developed the method for Fig 1, provided support for the experiments (Fig 1, ED1,2) and wrote the manuscript. BC carried out the calculations in the paper (SI3) and wrote the manuscript. PAB designed the study, interpreted the data and wrote the manuscript. SJF and JKH designed the study, interpreted the data, wrote the manuscript and directed the project.

Corresponding authors

Correspondence to Simon J. Foster or Jamie K. Hobbs

Competing interests

The authors declare no financial or non-financial competing interests.

Data Availability

The data that support the findings of this study are available in Online Research Data (ORDA) figshare from the University of Sheffield with the identifier DOI: 10.15131/shef.data.11798898.

Code Availability

The MATLAB code for determining glycan strand orientation can be found in Supplementary information 2.

Supplementary information

Supplementary information 1. Video showing a tomogram of a purified frozen hydrated *S. aureus* sacculus.

Supplementary information 2. MATLAB code for obtaining peptidoglycan strand orientation.

Supplementary information 3. Estimation of the critical pore size to maintain membrane integrity.

Extended Data

Extended Data Figure 1 | *S. aureus* cells and sacculi: cell wall fine structure and other cell wall components. **a**, Overview image of individual *S. aureus* wild type (WT) live cells trapped inside silicon holes. Topographic data scale (DS) = 1100 nm. **b**, Individual cell showing mature mesh covering the top surface, high pass filtered, filter size = 0.23 μm , vertical. **c**, Higher resolution image within **b** with blue dashed box denoting the location of **Fig 1b** in the main text. DS = 35 nm. **d**, Example of mesh from another cell. DS = 58 nm. **e**, *S. aureus* tarO mutant cells (this mutant lacks wall teichoic acids - WTAs) trapped in silicon holes (provided by NuNano – see Methods for sample preparation). DS = 2033 nm. **f**, Higher resolution image on an individual cell showing the mature mesh. DS = 580 nm, 3D details: Z aspect ratio = 1.0, Pitch = 16.5°, Plot type = height. **g**, Higher resolution image from **f** showing the mature mesh. DS = 34 nm, (comparison to **Fig 1b**). **h**, Concentric rings on tarO mutant (comparison to **ED2e**), DS = 46 nm. Direct comparison between the WT and tarO mutant shows that there is no substantial difference in the organization of the cell wall in the absence of WTAs and that the features observed in the WT are not WTAs. **i**, *S. aureus* ltaS mutant cells in an SH1000 background were purified and a sacculus with its external PG structure facing upwards is shown here. DS = 121 nm. **j**, Higher resolution image from within **i** highlighting the nascent PG structure of this sacculus with similar features to those seen in the WT. DS = 14 nm. **k**, Higher resolution image from within **i** corresponding to the mature PG structure of this sacculus with no apparent difference from the same structure observed in the WT cells (see

Fig 2b as an example). DS = 33 nm. This direct comparison between the WT and *ltaS* mutant shows that there is no apparent difference in the organization of the cell wall in the absence of LTAs (lipoteichoic acids) and that the features observed in the WT are not attributable to LTAs or WTAs so must be peptidoglycan. **l**, 3D view of the *S. aureus* cell that images **m-n** were taken from. DS = 398 nm, 3D details: Z aspect ratio = 0.5, Pitch = 35°, Light rotation = 36°, Light Pitch = 40°, Light Intensity = 60%, Plot type = mixed. **m**, Image showing periodic features along the glycan chain direction (white arrows pointing at single glycan strands clearly showing the periodicity). DS = 14 nm. **n**, Higher resolution image from **m** (dashed white square) showing the 3.7 nm periodicity. DS = 10 nm. **o**, Profile taken along the blue rectangle in **n**, showing a 4 nm separation between adjacent features. We suggest the periodic bumps are uncross-linked penta-peptide side chains presented at the surface every helical repeat. **p**, Schematic of the helical repeat of peptidoglycan, with statistics from 24 measurements similar to those in **o**, mean \pm s.d. is 3.7 ± 0.8 nm for the periodicity. This is in agreement with NMR data, (see reference 18 in the main text). The morphologies from **a-d** and **l** were also detected each in at least 5 other biological independent repeats, similar features to those in **m-n** in at least 3 biological repeats (see repository); from **e-g** two biological independent repeats were performed. **h-k** come from one biological repeat.

Extended Data Figure 2 | S. aureus live cell architecture. **a**, At the interface between the most recent division plane and the mature cell wall we find a sharp topographic step between the mature (mesh) and recently synthesised cell wall (concentric rings), see black arrows. DS = 535 nm, 3D details: Z aspect ratio = 1, Pitch = 21°, Light rotation = 103°, Light Pitch = 49°, Light Intensity = 70%, Plot type = mixed. **b**, Same image as **a** but processed with a Plane Fit at 3rd order showing the sharp interface in more detail. DS= 27 nm. **c**, profile from taken along the dotted black line in **a**, showing a sharp change in height at the interface between the mesh and the rings (see red arrow corresponding to red arrow head in **a**). **d-g** are a series of images, each from a different cell, showing the presumed time evolution of the ring architecture. Samples naturally contained cells with a distribution of times since their last division, and hence showing differing levels of maturation of the peptidoglycan at the extracellular surface of the most recent division plane. **d**, Recently revealed outer septal surface showing dense concentric rings. The blue dashed box shows the location of **Fig 1e** in the main text. DS = 18 nm. **e**, Image of a different cell showing what is probably the next stage of maturation. The rings are still prominent (white arrows), but show larger spacing, greater height variation and pores have appeared in the surface. Features oriented approximately along the radial direction are also apparent. DS = 23 nm. **f**, A different cell showing the subsequent stage where, underneath the rings, the pores of the mesh have started to appear. DS = 38 nm. **g**, The last

stage of maturation of the cell wall is the completely disordered mesh without any traces of former ring structures. DS = 30 nm. The morphologies from **a-b** were also detected in at least 1 other biological independent repeat (see repository) and from **d-g** were also detected each in at least 2 other biological independent repeats (see repository).

Extended Data Figure 3 | Mechanistic insight into peptidoglycan hydrolysis and synthesis.

a, Sacculi of *S. aureus* WT imaged in air, with different fragments containing single layers of PG (green dashed arrows) and double layers (black dotted arrow), DS = 75 nm. **b**, Sacculi from *S. aureus* sagB mutant in an SH1000 background imaged in air. The fragments have two distinct regions with different thicknesses (pink and orange arrow heads). These are distinct from the double layer fragments (black dotted arrow), DS = 75 nm. **c**, Graph comparing the thickness of the cell wall in air and liquid between the sagB mutant and the wild type. The box-plot consists of boxes from 25-75 percentile, middle line represents the median, black star represents the mean value, error bars are maximum/minimum values excluding any outliers (using 1.5 inter-quartile range). The two different regions of the sagB cell wall are separately binned and labelled 'sagB thin' and 'sagB thick'. Measurements were taken using the same approach as the values for graph **Fig 2k** in the main text and **ED4**. Number of sacculi measured $n = 25$ for each bin. Mean values \pm s.d. are: 'sagB thin air' = 12 ± 3 nm, 'sagB thin liq' = 24 ± 7 nm, 'sagB thick air' = 21 ± 1.5 nm, 'sagB thick liq' = 42 ± 5.7 nm, 'WT air' and 'WT liq' corresponded to the same values as **Fig 2k** (left data, PG+WTA). All measurements in liquid were performed in buffer 300 mM KCl + 10 mM Tris, pH = 8. **d**, *S. aureus* sagB mutant sacculus in liquid with its external surface facing upwards. This sacculus is clearly divided into two sections, the region on the left is thinner than the region on the right. This irregularity in height was visualised in several sacculi from cells with this mutation. DS = 64 nm. **e**, Higher resolution image from the thicker section in **d** corresponding to the finer mature CW architecture. This mesh is still in an early transition from rings, with some features reminiscent of rings visualised following the same orientation (blue arrows). These sorts of structures are uncommon on WT sacculi at the same stage in the cell cycle (exponential phase $OD_{600} = 0.5-0.7$). However, in the sagB mutant it was more common to find this early transition from rings to mesh. DS = 11 nm. **f**, Higher resolution image from the thinner section in **d** showing the finer nascent CW architecture (i.e. rings). Inset shows a lower resolution image of the ring architecture in a different sacculus. The features from this image are not significantly different from WT nascent PG architecture, such as **Fig 2d** in the main text. However, almost every sacculus containing nascent architecture in the sagB mutant had this part of the cell wall being thinner than the rest of the sacculus, something not seen in the WT. DS = 9 nm, inset DS =

29 nm. **g**, Sacculus fragment with the inner CW architecture facing upwards, DS = 14 nm. **h**, Higher resolution image from **g** showing the fine inner structure of the *sagB* mutant, with no clear difference from the very tight and disordered structure seen in WT sacculi (see **Fig 2f** from the main text for example). DS = 4 nm. **i**, Sacculi from *S. aureus* *pbp3* mutant cells in an SH1000 background. Here we show the fine external structure, with no apparent difference between this and the *S. aureus* WT mature external structure. It is important to highlight that PBP3 is not an essential peptidoglycan synthesis enzyme, and the cells can survive without it and still maintain their spheroid shape. DS = 55 nm. **j**, The fine structure of an *S. aureus* *pbp3* mutant sacculus with the internal peptidoglycan surface exposed, which is similar to that seen in wild type *S. aureus*. DS = 4 nm. **k**, Sacculus from *S. aureus* *pbp4* mutant cells in an SH1000 background showing nascent peptidoglycan structure, with the concentric rings facing upwards. It is important to highlight that PBP4 is not an essential peptidoglycan synthesis enzyme either, and the cells can survive without it and still maintain their spheroid shape. DS = 28 nm. **l**, Higher resolution image taken within **k** showing the fine structure of the nascent peptidoglycan surface, the concentric rings. There is no significant difference compared to the *S. aureus* WT nascent structure, except the fraction of sacculi with rings in a random area is higher in this sample than WT. DS = 8 nm. **m**, Sacculus showing a small area of the mature peptidoglycan structure (green long arrow), with its external surface facing upwards, the rest of the sacculus is covered by concentric rings already in the late phase of the transition to mesh (black short arrow pointing to the centre of the concentric rings, boundary with the mature structure, red dashed line) and the newest generation fragment with rings (blue arrow head, boundary with oldest rings marked with red dotted line). It is important to highlight this is the first time two perpendicular planes of rings have been visualized at exponential phase in our experience. $OD_{600} = 0.6$. DS = 79 nm. **n**, Higher resolution image from **m** showing the fine structure of the mature external CW of an *S. aureus* *pbp4* mutant, with no apparent difference between this and the *S. aureus* WT mature external structure (see **ED1** and **Fig 2b** from the main text). DS = 44 nm. **o**, Sacculus showing the fine internal structure of *S. aureus* *pbp4* mutant cell wall, with no apparent difference compared to the *S. aureus* WT internal peptidoglycan architecture (see **Fig 2f** from the main text). DS = 10 nm. These data show that removal of non-essential PBPs makes only relatively minor differences to the wall architecture.

Extended Data Figure 4 | S. aureus sacculi. **a**, Height image of the same sacculus shown in **Fig 2a** in the main text. This sacculus has been broken on the left side and emptied of all of the cell's contents, allowing the difference in PG structure between the internal and external surfaces to be clearly seen. Imaging buffer: 10 mM Tris pH 7.8 + 300 mM KCl. DS = 192 nm.

b, Same sacculus as **a** but imaged in air (dried with nitrogen flow). DS = 84 nm. **c**, Higher resolution image from **a** taken in buffer showing the mature mesh, white arrows (1-6, lower regions on the image), blue arrows (7-13, higher regions on the image). DS = 33 nm. **d**, Image of the same region of mesh as in **c** but in air. This morphology has been previously termed “knobbles” (see reference 7 in the main text). Arrows were manually placed to point to the corresponding features as 1-13 in **c**. DS = 11 nm. **e**, Image of sacculus fragment in buffer conditions 10 mM Tris pH 7.8 + 300 mM KCl. The height of the sacculus (32.4 nm) was measured using the 1D statistical analysis from Gwyddion™ software (see details in Methods). **f**, The same sacculus fragment as **e** but imaged in air with an overall height of 17.5 nm measured in the same way as **e**. Both images (**e**, **f**) have the same data scale (DS = 65 nm). The same process was repeated with 24 other sacculi to produce the thickness data for **Fig 2k** in the main text, using a positioning marker either on the sample or substrate beneath to enable the same fragments to be located in both air and liquid. **g-j**, Analysis of the septation process. **g**, A graph showing decreasing aperture size in the septum with constant septum diameter ($n = 5$ measures) of septation aperture for each septum shown in circles. The centre values represent the mean value and the error bar the maximum value excluding outliers. Septa 2, 3 and 5 being **h** to **j** respectively. Images **h-j** show different stages of septal growth, each image collected from a separate *S. aureus* sacculus. Images are presented in order of apparent septation progress, with the internal aperture in the middle of the septa getting smaller for cells at later stages of septation. DS: **h**, 548 nm, **i**, 512 nm, **j**, 627 nm. The area corresponding to **Fig 2h** in the main text was taken from the blue dashed box in **h**. The black arrow in **j** indicates the internal aperture in the centre of this nearly completed septum. Images **h-j** were taken from cells grown at $OD_{600} \sim 0.1$, because this condition provided a higher number of partially-formed septa in the sample. **k**, Higher resolution image from **a** of the internal structure of *S. aureus* cell wall, showing a randomly orientated dense mesh. DS = 10 nm.

Extended Data Figure 5 | Quantitative analysis of pores. **a**, Image **ED2g** of the mature PG structure from an *S. aureus* live cell image represented in 3D and then tilted. The lateral resolution is lost and no clear information about the pores is visible with this representation. Therefore, a new analysis method was designed. The first step is to measure the maximum depth of this 3D image, the Z_{max} is calculated neglecting the areas below 0.3% and above 99% because they might contain artefacts and signal errors from the AFM. **b**, a two dimensional sectioning process is performed in the XY plane going down from Z_{max} highlighting a set of certain depths. **c**, Slices were taken at intervals of approximately 3% of the total Z_{max} , including

slices with the selected depths from **b**. **d**, All slices of different depths were super-imposed on top of the original image **ED2g**, five of the slices are highlighted in different colours (blue = 5 nm, green = 10 nm, orange = 15 nm, purple = 20 nm and white = 23 nm) showing the different areas covered by different depths. This is the complete image from which **Fig 1c** in the main text was cropped. **e**, After converting all the slices into a stack of images in '.tiff' format, AvizoLite™ software was used to represent the pores' shape in 3D (view from the bottom) and the chosen set of depths were marked with the same colours as in **d**; a black arrow highlights the deepest pore in this image. **f**, This procedure was repeated for the mature PG structure from *B. subtilis* live cell, image **ED7d**. The 2D version of **f**, analogous to **d**, is shown in **Fig 3d** in the main text. Again the deepest pore in the 3D representation is marked with a black arrow. **g-h** Show a direct comparison of lateral slices in the XZ plane, so that the lateral profile of the pores can be visualised. Peptidoglycan is coloured grey in these images. The lateral slice from *S. aureus* is extracted from the red dashed line marked in **d** and for *B. subtilis* it corresponds to the black dashed line in **Fig 3d** in the main text. **i-k** show the steps followed to quantitatively compare the area of the pores on the outside of the cell and the inside of purified peptidoglycan. **i** shows the raw data extracted from the AFM. **j**, The image has been processed with the Nanoscope Analysis software (3rd order Plane-fit) to remove the offset, tilt and curvature of the cell. The image has been converted to greyscale, and a despeckle filter (3x3 median filter) has been applied with ImageJ/Fiji (see reference 38 in Methods). **k**, A 2D slice in the XY plane was made at a depth of 50% of Z_{\max} for 6 images of live *S. aureus* and 4 images of internal *S. aureus* sacculi using the ImageJ/Fiji threshold tool. Slices were then binarised with pores in black and peptidoglycan in white. The "analyse particle" tool from ImageJ/Fiji was used to measure the pores. This outputs a list of individual pores with their associated area and a number for each pore. **l**, In some cases, in particular when several pores lie within a larger depression on the surface, pores are artificially merged. These were manually removed from the dataset by comparing the binary image with the grey scale image. Correctly assigned (retained) pores are shown in blue, three artificially merged (discarded) pores are shown in black. **m-o**, Histograms of pore area. **m**, Pore area histogram calculated for 310 pores from 6 separate images for the external surface of live *S. aureus* cells. The bin width is 150 nm². **n**, A subset of the same dataset as **m** (denoted by the blue dashed box) binned at 10 nm² intervals. **o**, Pore area histogram calculated for 158 pores from 4 separate images of the internal surface of *S. aureus* sacculi, binned at 2 nm² intervals. The distributions of pore area are non-normal and positively skewed for both the internal and external surfaces. 90% of the pores in the external surface have area < 900 nm² (grey dashed line in **m**). For the internal surface, 90% of the pores have area < 47 nm² (grey dashed line in **o**). The mode and

quantiles Q_{1-3} (25, 50 and 75% respectively) are marked on the figure distributions in **n** and **o** with dashed lines.

Extended Data Figure 6 | Tomogram of purified frozen hydrated *S. aureus* sacculus. *S.*

aureus WT cells were purified and treated with HF to remove all WTA, so that only a pure PG sacculus was imaged. Tomograms were captured of five sacculi, an example of a single sacculus is given in Supporting Information (see 'Video_SI1'). **a**, Shows a 13 nm thick tomogram slice from the first stop point on 'Video_SI1' which corresponds to the external CW surface showing disordered structures throughout the area of the sacculus (see blue arrows). **b**, shows a 13 nm thick tomogram slice from the second stop point on 'Video_SI1' corresponding to the other side of the CW, the smooth internal structure which is in agreement with the AFM data presented in **Fig 2**. **c**, shows an intermediate 13 nm thick tomogram slice between **a** and **b** where the outline of the CW exterior surface is visualized showing a disordered structure presumably formed by pores. **d**, as **c** with the exterior surface highlighted in yellow, examples of individual pores analyzed are indicated by blue arrows. **e**, Graph plotting the area of each pore vs the cumulative fraction of the total pore area of all pores analysed. The blue dots correspond to measures from the AFM images of *S. aureus* cells, measured at a height of 50% of the total image height scale (data also presented in **Fig 2i**), the black dashed line is the linear fit to these data. The orange squares are individual measurements of pore diameter from image **d** converted into pore area by assuming the pores are circular, the black dotted line is the linear fit to these data, showing a similar slope to the AFM data. Red stars show 50% of the cumulative area, i.e. half of the total pore area consists of pores smaller/larger than this value. The values calculated from the linear equations for both types of data are: 39 nm for AFM data and 42 nm for the Cryo-EM data. This slight difference is most likely due to the lack of smaller pores analysed by Cryo-EM, which is highlighted with a transparent green area in the graph. Total pores analysed by AFM were $n = 311$, from $n = 6$ images and by Cryo-EM were $n = 30$, from 1 image. For more details on the 'Video_SI1' see SI1. **f**, The same tomogram slice as **ED6a** highlighting a region of the sacculus that is smooth on both the inside and the outside. Cryo-EM does not discern the ring structure as it views in transverse section, but we suggest that this region of the sacculus is most likely made up of rings. **g**, Shows the region highlighted in yellow in **f**, which has been traced with a spline function which was then used to straighten the section. **h**, Shows the same tomogram slice as **ED6a** highlighting in yellow a region with a rough external surface, which we suggest corresponds to the mesh architecture observed with AFM. **i**, Shows the yellow region of **h** straightened as in **g**. **j**, AFM image of a sacculus showing two distinguishable areas

(reproducing **Fig2c**), the top part consists of a smooth surface with occasional pores, where the glycan strands are organized as concentric rings. On the bottom part of the sacculus, the mature CW shows a highly topographic surface. **k**, Shows **f** cropped to the same size as the AFM profile shown in **l**. **l**, AFM profile in yellow from the red dashed line in **j**, showing an almost flat surface. **m**, Shows **i** cropped to the same size as the AFM profile in **n**. **n**, AFM profile taken along the blue dotted line in **j**. We note the qualitative similarity between the two data sets, despite the very different contrast mechanisms of the two techniques. **o**, Shows an example tomogram slice from a tomogram of a different sacculi. **p**, The region of the cell wall highlighted in yellow, straightened as in **g** above. **q**, Another example AFM image of the mesh architecture. **r**, The area indicated with the blue box in **p**, cropped to the same size as the AFM line profile below, highlighting the rough texture of the external cell wall. **s**, Profile taken along the blue dashed line in **q**.

Extended Data Figure 7 | B. subtilis live cells and sacculi. **a**, High pass filtered image (filter size 0.2 μm , horizontal) of *B. subtilis* cell cylinder in exponential phase attached to a Cell-Tak coated substrate, inset (I) shows the unfiltered height data. DS = 1417 nm. **b-d**, Higher resolution images of mature cell wall (mesh) within image **a** in locations marked with white dashed squares. DS = 31 nm, 27 nm and 21 nm respectively. The external surface of *B. subtilis* is covered by disordered mesh all along the cylinder with the exception of the newly synthesised poles (which have concentric ring architecture). **e**, Image of a sacculus from a *B. subtilis* cell, showing the internal surface of a pole. We can differentiate between poles and completely formed septa because of the folded material on top (blue arrow). No septa were observed with this feature. DS = 130 nm. **f**, Higher resolution image from within **e** showing the fine structure of the internal pole, similar to the internal structure of *S. aureus* suggesting that this architecture is characteristic of the spherical part of Gram positive cells. DS = 87 nm. **g**, External part of the pole facing upwards with the interface between the pole and the rest of the cylinder indicated by blue arrows. DS = 118 nm. We presume this image corresponds to a mature pole, and that the concentric rings have become mesh, suggesting that the structural reorganization in time from rings to mesh also occurs in *B. subtilis* poles. **h**, Example of newly synthesised pole facing upwards with a sharp interface between the pole and the rest of the cylinder (blue arrows). This pole displays very tight concentric rings in contrast to **g** and similar to **Fig 3e-f** in the main text. DS = 800 nm. **i**, The same image as **h** but processed with Gwyddion and JPK software (flattened to 0th order with mask drawn manually over the sacculus, path level to remove lines), allowing the concentric rings (white arrow) to be visualised more clearly. The results from images **e-i** support a common process of synthesis and maturation of cell wall on the spherical parts of Gram positive bacteria in both spherical and rod-shaped species. Images **e-i** were taken with a JPK NanoWizard 3 in QI mode (see

Methods). Images **e-h** were processed with Gwyddion (see reference 34), image **i** was processed with JPK data processing software, the colour palettes are different. **j**, Image showing two fragments from *B. subtilis* sacculi. The one on the left corresponds to the internal structure facing upwards (white arrow head), the fragment on the right has the external structure of the cylinder, mesh, facing upwards (blue arrow). The assumed cylindrical axis is marked (red dashed arrow). DS = 118 nm. **k**, Higher resolution image from within **j** of internal cell wall. Some larger pores are visualised here and there is some predominant orientation indicated by the angle distribution of the fibres shown in the inset (**l**), in agreement with the cylindrical axis (red dashed arrow). The method for obtaining these distributions is explained in **ED8**. DS = 46 nm. **l**, Example of *B. subtilis* sacculus fragments showing the two different structures: the internal cell wall in the two fragments (white arrow heads) and the top part of the cylinder corresponding to the external cell wall (blue arrow). DS = 146 nm. The distinction between this image and that shown in **j** is that these fragments are part of the cylinder that once belonged to the same cell, the blue dashed box marks the area corresponding to **Fig 3i** in the main text, the assumed cylindrical axis is marked (red dashed arrow). **m**, Higher resolution image from **l** of internal cell wall. This strongly aligned structure (see Inset, **l**) is the most commonly found in these sacculi in contrast with **k**. As the fragments in **l** are not totally broken, we assume this will be more similar to the native structure of cell wall. DS = 19 nm. **n-p**, Images of the different structures from *B. subtilis* sacculi that have been HF treated so the WTA have been removed: **n**, mesh seen on the external surface (DS = 30 nm), **o**, strands inside (DS = 30 nm), circumferential axis direction given by the red dotted line, strand orientation Inset, **l**) and **p**, partially-formed septum (DS = 130 nm). This shows that none of the previous structures were due to teichoic acid organization, which is consistent with our findings for *S. aureus* cells.

Extended Data Figure 8 | B. subtilis strand orientation analysis and mechanistic insights – a, *B. subtilis* mreB mbl mreBH, rsgI mutant sacculus image of the internal structure of cell wall, with a defined ridge (green arrow). This mutant lacks the MreB family of proteins, which leads to a spheroidal shape. DS= 411 nm. **b**, Higher resolution image from **a** showing the fine structure of the internal surface of a *B. subtilis* mreB mbl mreBH, rsgI mutant sacculus, with a disordered structure (see Inset, **l**, indicating a broad distribution of strand orientations) similar to the internal structure of *S. aureus*, suggesting that when Gram positive cells cannot maintain a rod shape, no cylindrical orientation is required. DS = 52 nm. **c**, Data used to obtain the orientation distributions for the glycan strands. Lines were hand drawn over the images along the clearly visible strands, using short straight strokes. A custom MATLAB routine (S12)

was then used to obtain the orientation distribution of these lines. The routine successfully recognised ~ 70% of the lines and determined their orientation. **d**, The mutations of the MreB family, shown in **a-c**, was created in a *B. subtilis* rsgI background strain. We prepared a purified sample from this *B. subtilis* rsgI mutant as a control. This image corresponds to the internal CW structure. DS = 76 nm. **e**, Higher resolution image from within **d** showing glycan strand orientation along the short axis of the rod morphology of the bacteria (dashed red arrow and inset, **l**). This sample had the same characteristics and structures as the WT strain. DS = 23 nm. **f**, Data used to plot the orientation distribution rose from inset in **e**. **g**, As an additional control, a sacculi sample of *B. subtilis* WT was grown as the mutants. This image shows another internal CW structure from a broken sacculus. DS = 125 nm. **h**, Higher resolution image from within **g** showing glycan strand orientation cylindrical along the short axis of the rod morphology of the bacteria (see dashed red arrow and inset, **l**). DS = 16 nm. **i**, The same strand orientation analysis as shown in **h** was applied to the external surface of *B. subtilis* cells (**Fig. 3c** in the main text), the angle distribution is broad (inset, **l**), indicating the glycan strands on the external surface have no predominant orientation in contrast with the internal surface. **j**, Data used to plot the orientation distribution rose from the inset in **i**, using the same procedure as **c** and **f**. This experiment provides mechanistic insight into the cylindrical orientation architecture in the inside of the rod-shaped of Gram-positive species *B. subtilis*. The protein complex of MreB, Mbl and MBH is vital for the synthesis of the peptidoglycan in this cylindrical architecture²²⁻²⁴.

Extended Data Figure 9 | B. subtilis septa – This figure compares images of *B. subtilis* cell wall fragments acquired in liquid with images of the same fragments acquired in air, and allows our current findings to be understood in the context of our previous study (reference 21 from the main text). **a** and **b**, *B. subtilis* septa at different stages of formation, imaged in liquid. DS = 70 nm and 158 nm respectively. In both cases a disordered mesh structure is apparent with pores penetrating deep into the cell wall. **c** and **d**, corresponding images from the same septa as **a**, **b** in the same orientation in air. DS = 31 nm and 60 nm respectively. Some features that were observed in our previous work, such as the concentric rings around the circumference of the septa (green arrow heads), and the ridges around the outer diameter of the septa (blue arrow), were identified. We attribute these features to the superposition of the mesh structures on both sides of the septa, with the concentric rings formed in the middle between them, coupled with the influence of differential drying. The experiment of correlating *S. aureus* sacculi in ambient and liquid environment (**ED4**) to measure the difference in thickness, was repeated for *B. subtilis* sacculi fragments and also showed a significant difference. **e** and **f**,

Examples of single layer fragments, marked 1 and 2, imaged in water and in air. The thickness of each individual fragment was measured using the 1D statistical analysis from Gwyddion™ software (see details in Methods). **g**, Graph showing the thickness for 19 sacculi measured in both air and liquid. There is a significant increase in thickness in liquid after a two-tailed paired t test was performed (p value = $1.2 \cdot 10^{-9}$, see Methods). The box-plot consists of boxes from 25-75 percentile, middle line represents the median, black star indicates the mean value, error bars are maximum/minimum values excluding any outliers (using 1.5 inter-quartile range). Mean value \pm s.d. are: 'air' 9 ± 1 nm and 'liquid' 34 ± 5 nm. These results are in agreement with sacculi thickness measured by TEM of *B. subtilis* (Fig 4 in reference 5 in the main text). **h**, Higher resolution image from **Fig 3j** in the main text. The internal surface of this partially-formed septum is composed of randomly orientated mesh. Large pores are present going partially through the cell wall (blue arrows). DS = 137 nm. **i**, In contrast to **h** in this partially-formed septum most of the material has been synthesised already, the pores are not as deep or wide as in **h** (yellow arrows). DS = 160 nm. These two septa differ in the size of their aperture by 100 nm, meaning they are probably representing consecutive stages of septal formation. The structural difference between them suggests that there is more than one type of synthesis happening simultaneously: one happening at the leading edge of the aperture making it smaller, the other responsible for in-filling the pores going partially through the cell wall as seen in **h**, finally resulting in the tighter mesh seen in **i**.

Extended Data Figure 10 | Gram positive bacterial cell wall molecular architecture schematic – Schematic diagram showing proposed peptidoglycan organisation derived from AFM imaging for both *S. aureus* and *B. subtilis*. Drawings top-centre and bottom-left indicate areas of distinct morphology within the cell wall during the division process. Insets show schematised representative AFM images of the different architectures within the cell wall, all displayed at the same scale.

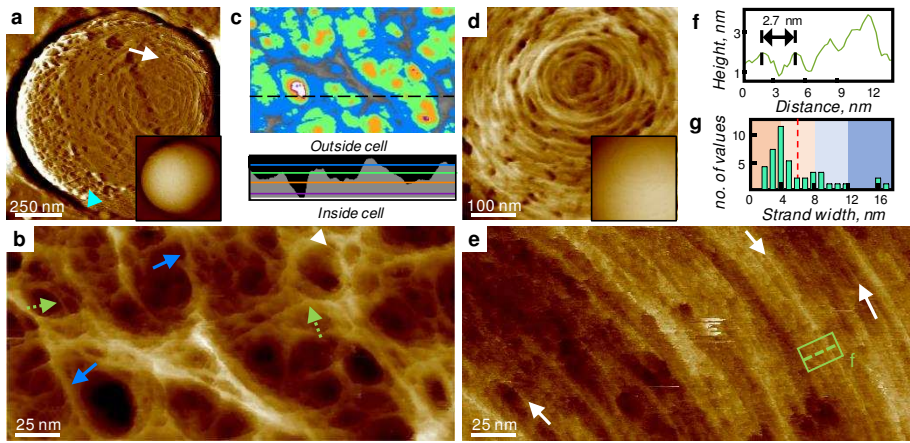


Figure 1

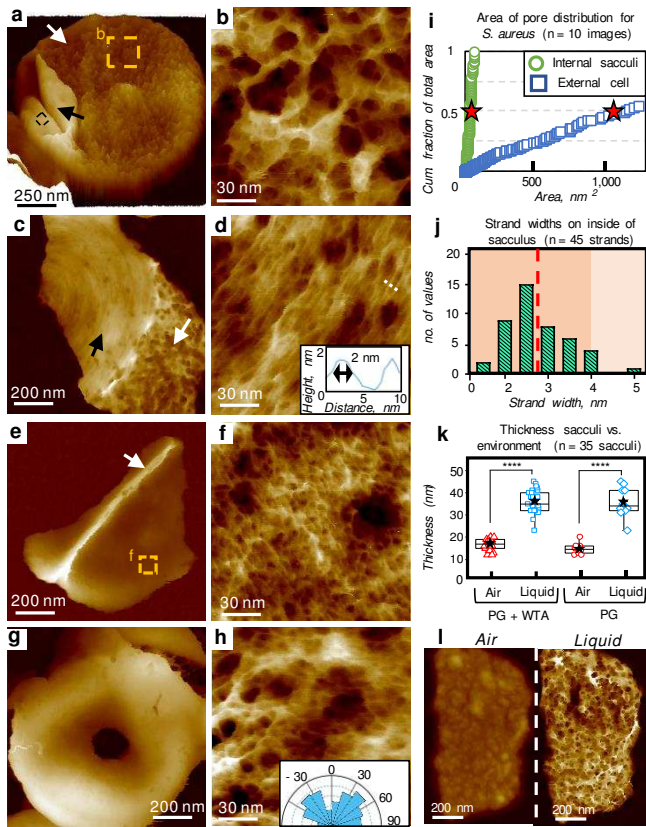


Figure 2

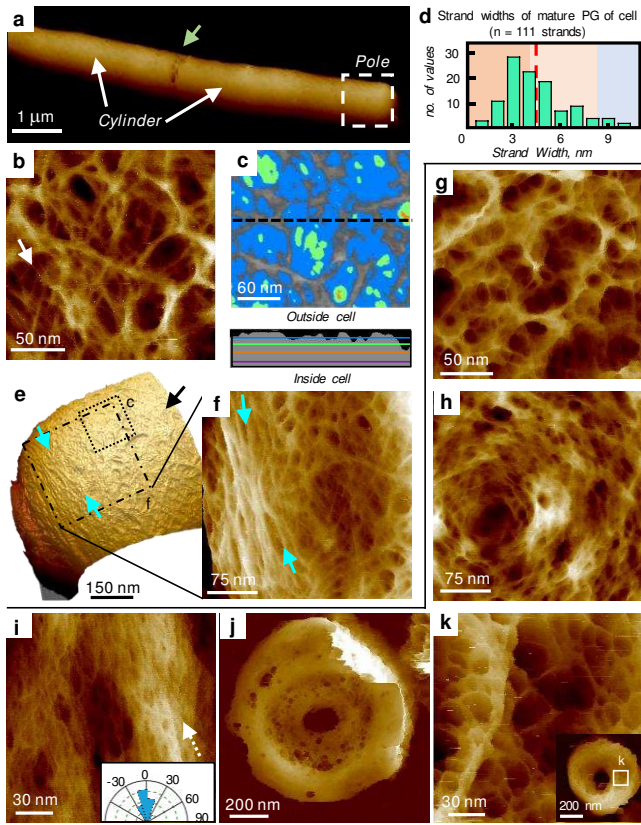
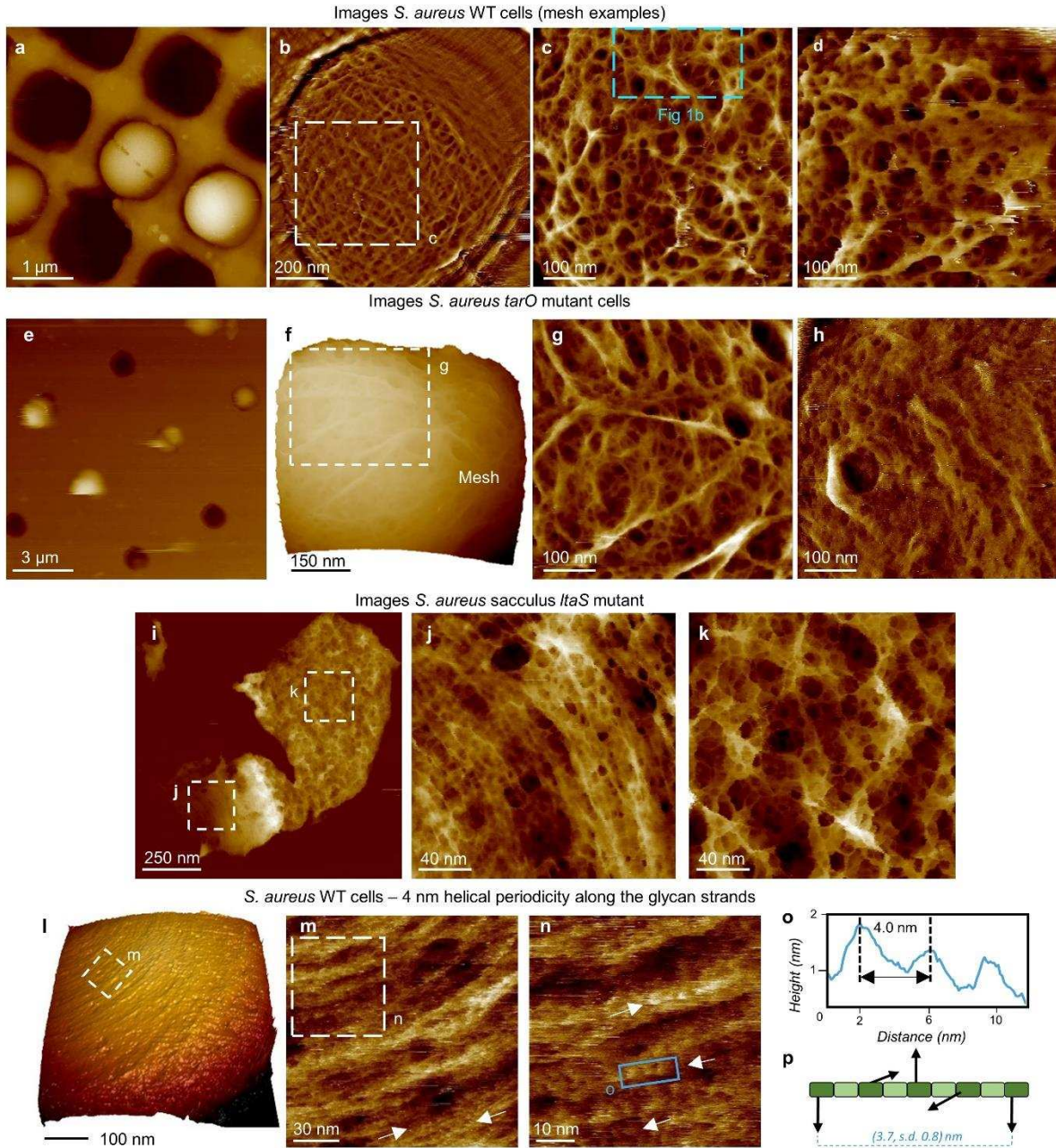
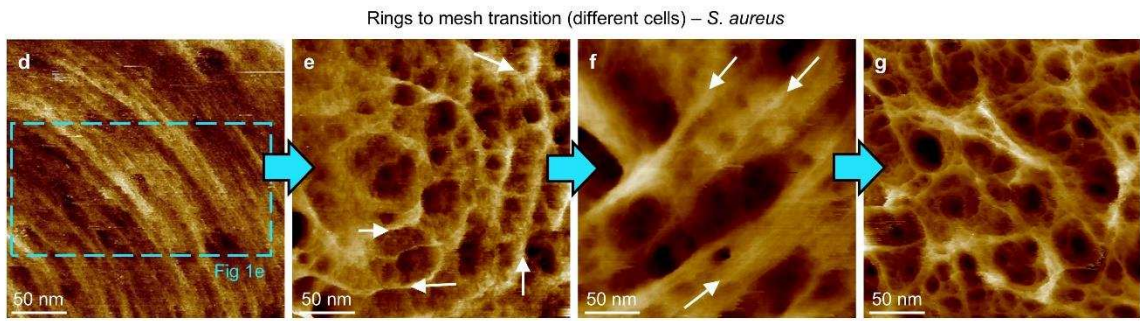
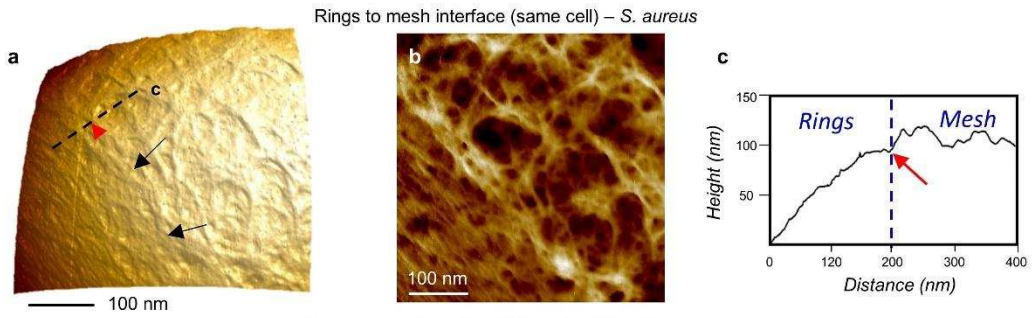


Figure 3

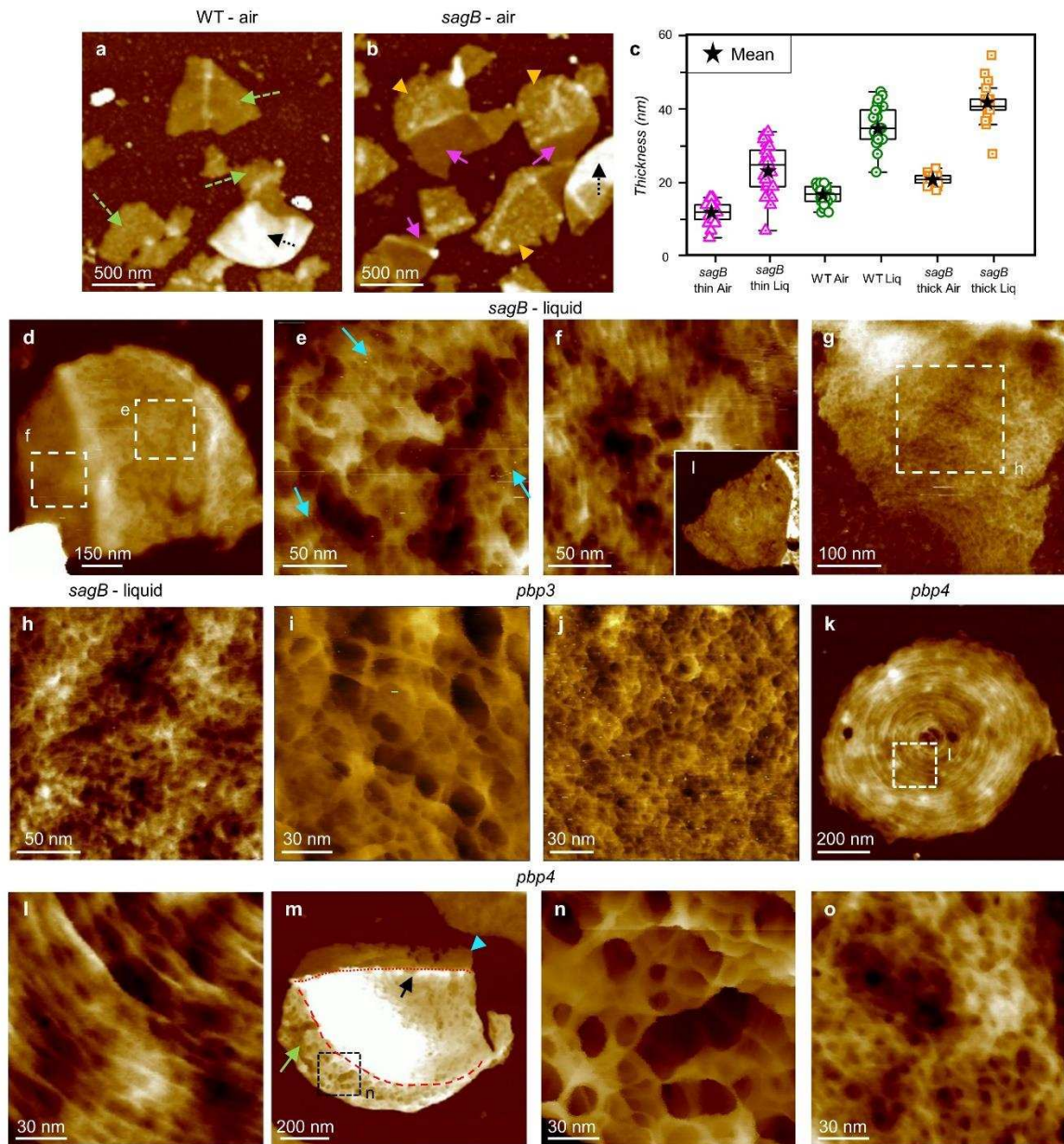


ED Figure 1

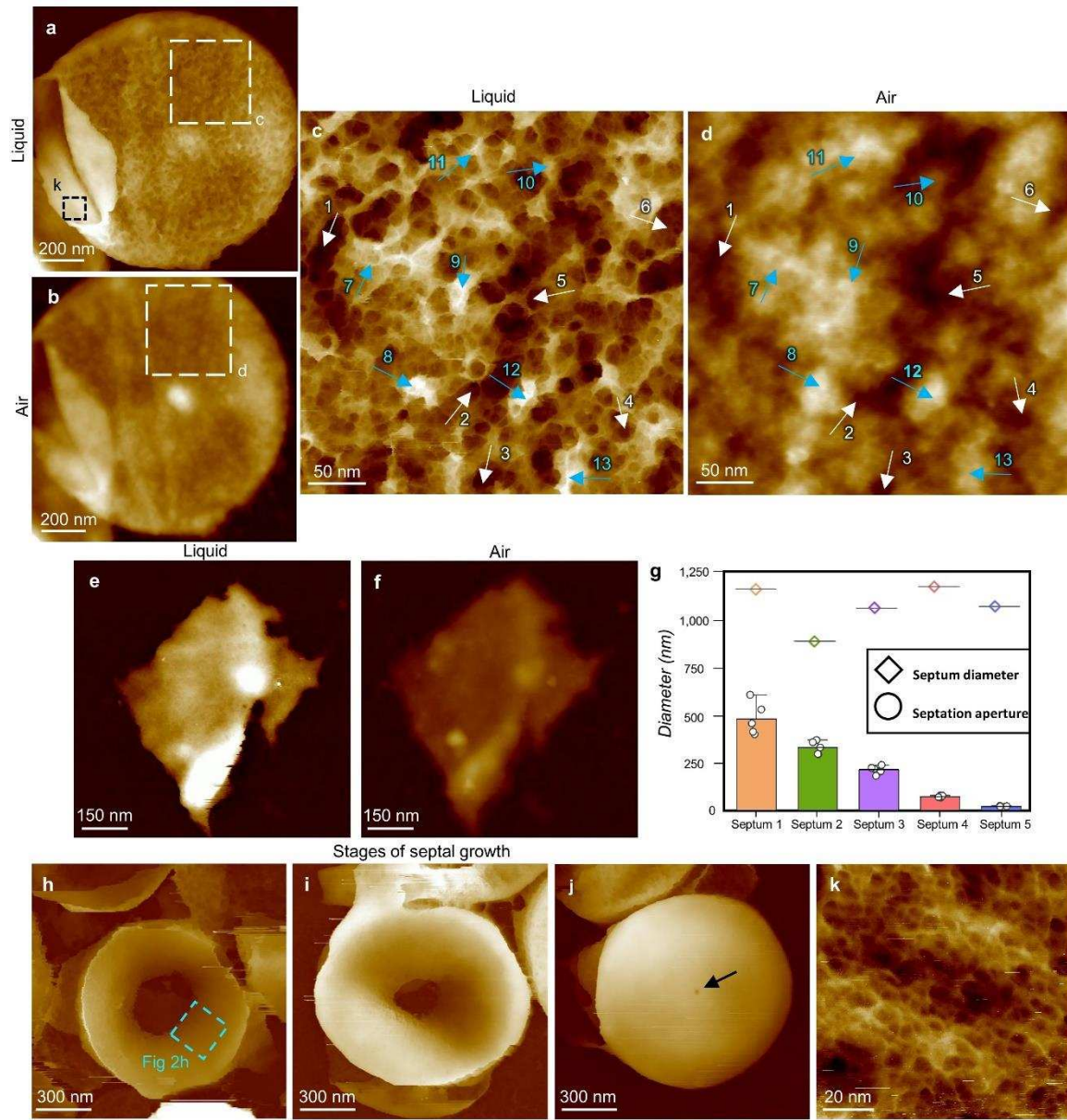


ED Figure 2

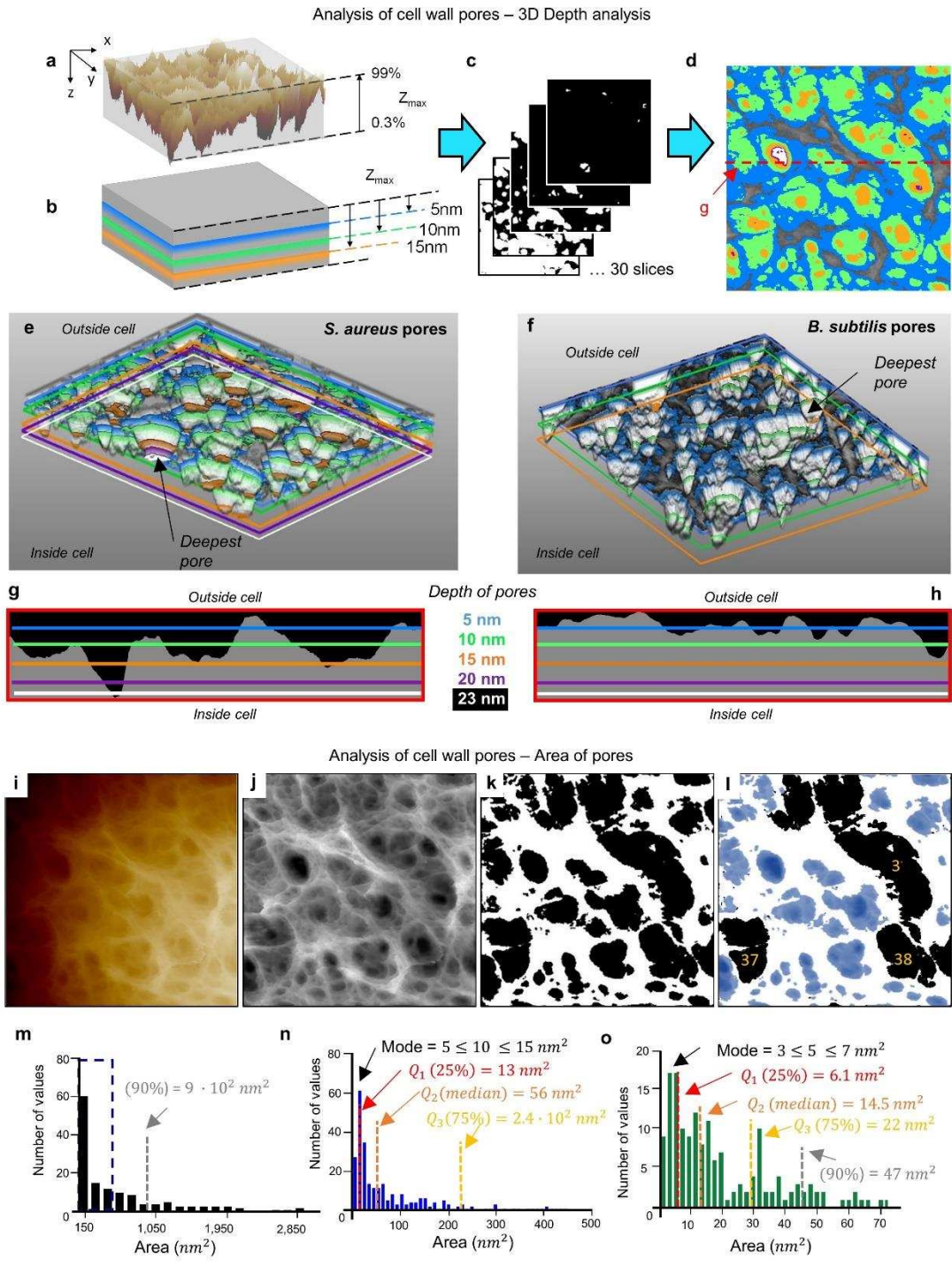
S. aureus sacculi – mechanistic insights into peptidoglycan hydrolysis and synthesis *sagB*, *pbp3*, *pbp4*



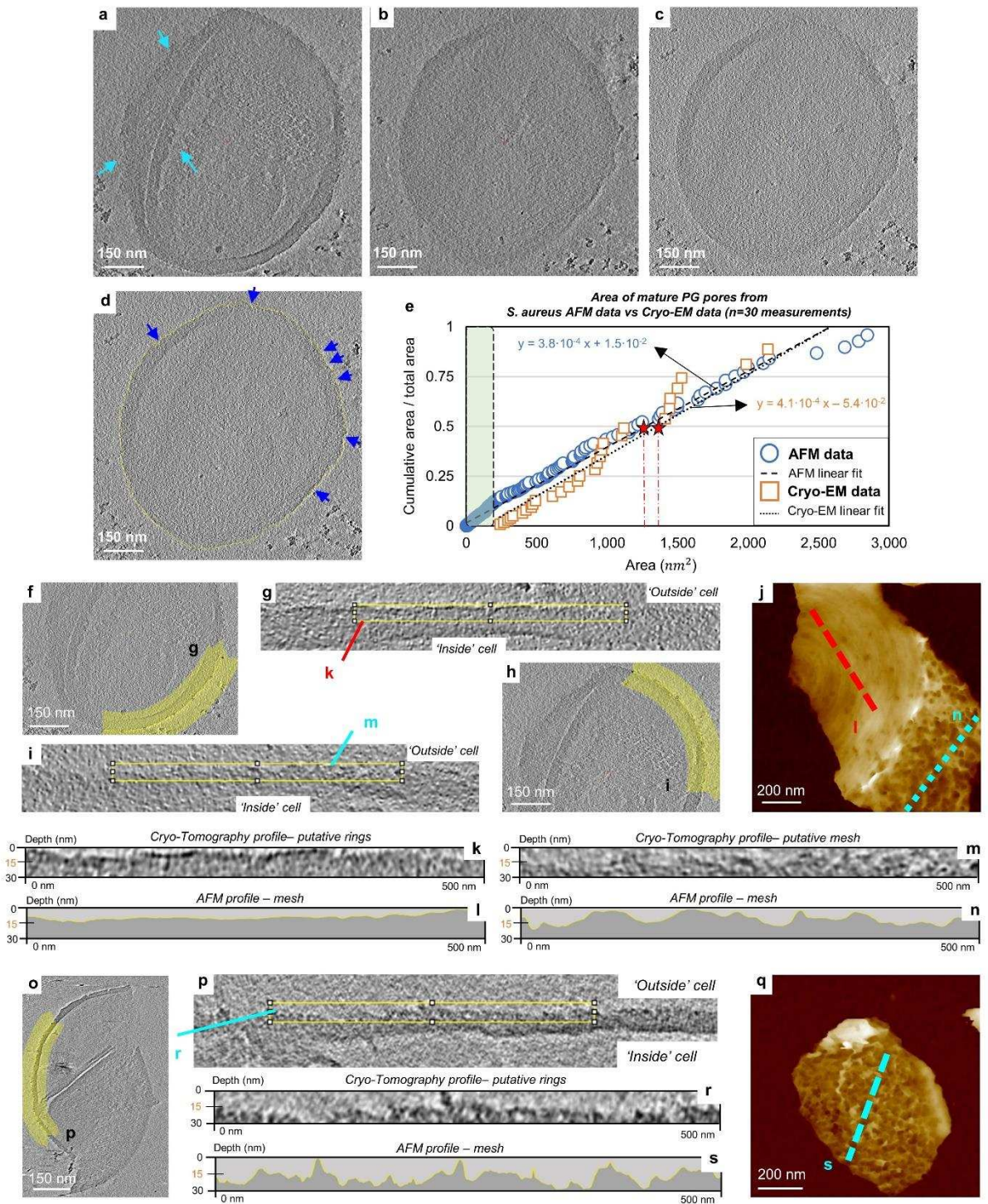
ED Figure 3



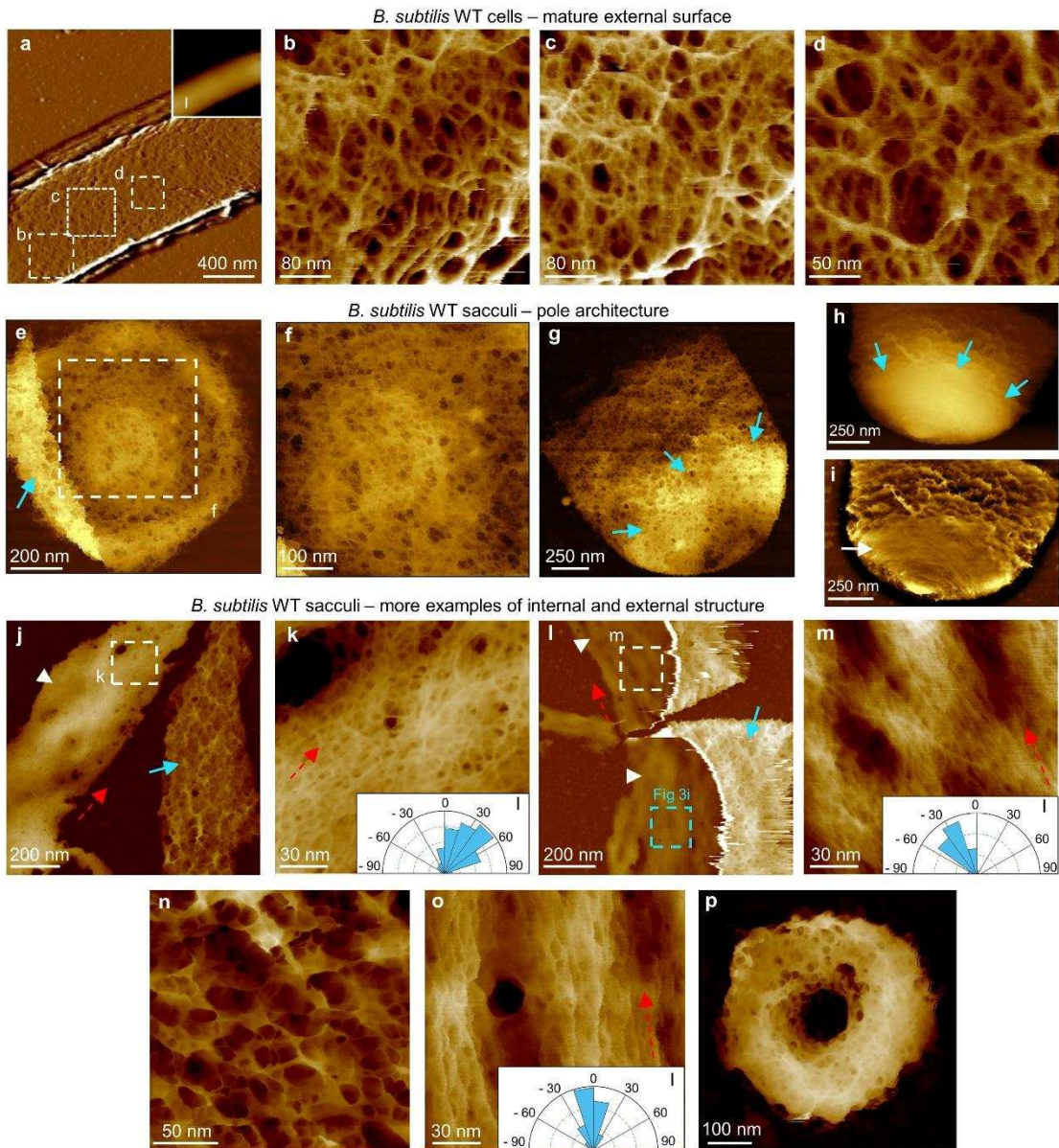
ED Figure 4



ED Figure 5

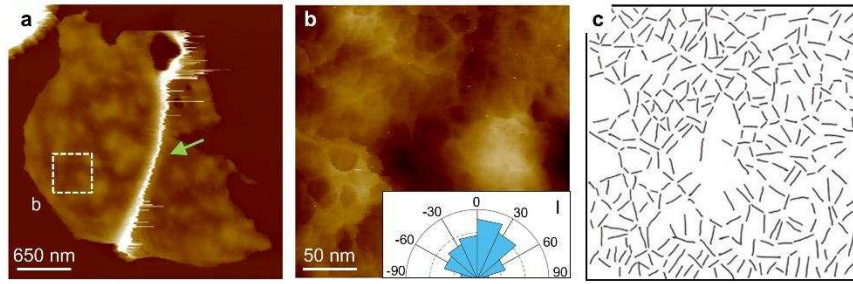


ED Figure 6

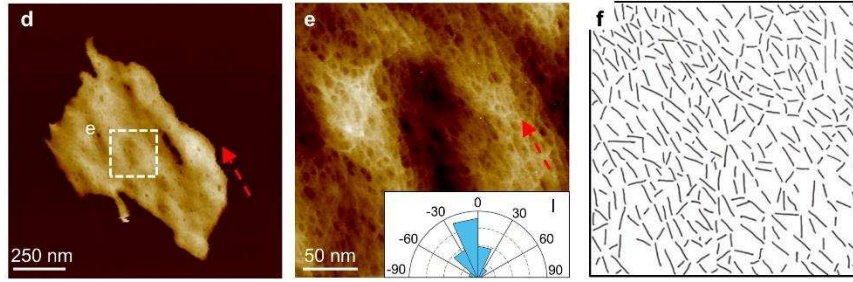


ED Figure 7

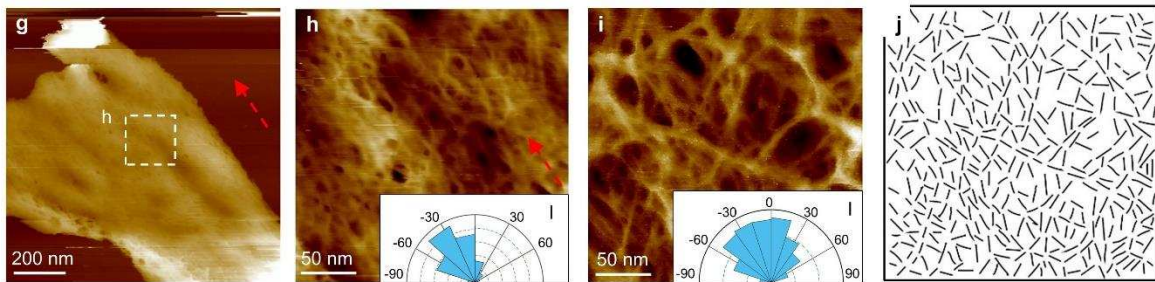
B. subtilis mreB, mbl, mreBH, rsgI sacculi



B. subtilis rsgI sacculi

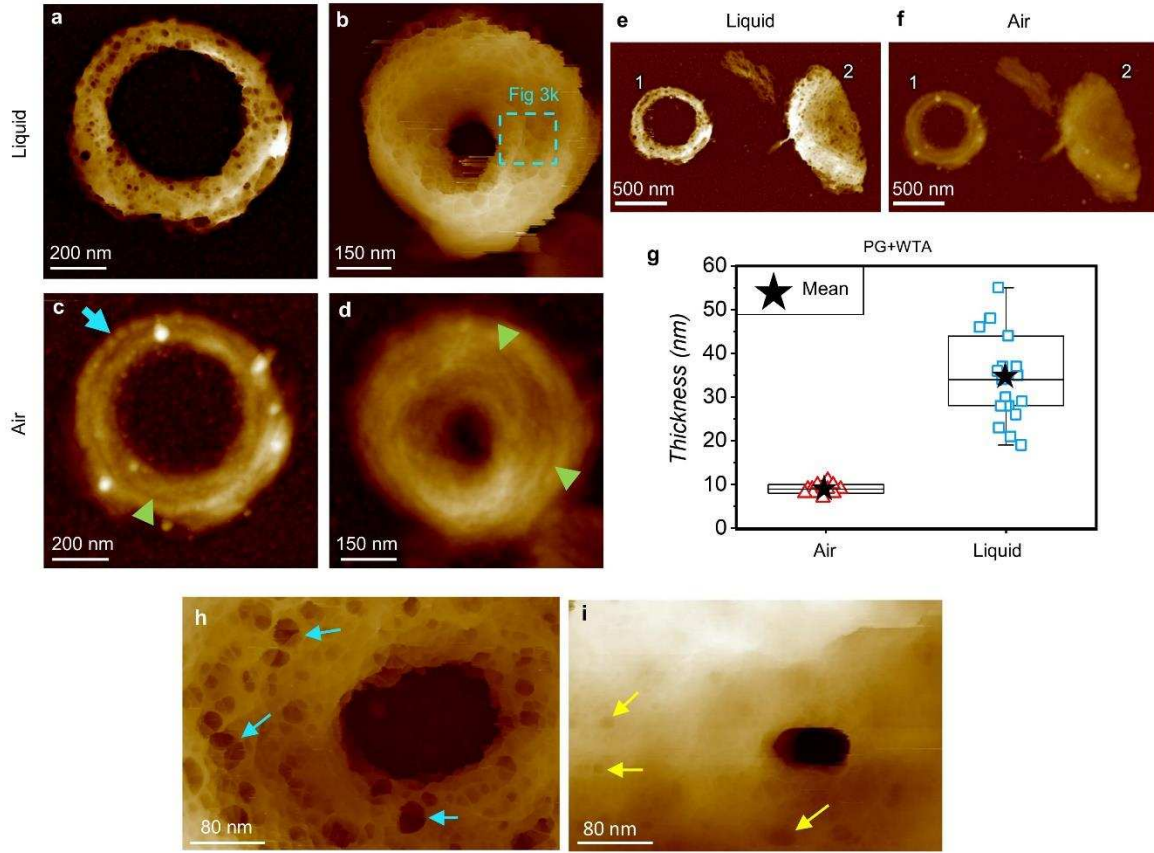


B. subtilis wild type (control)

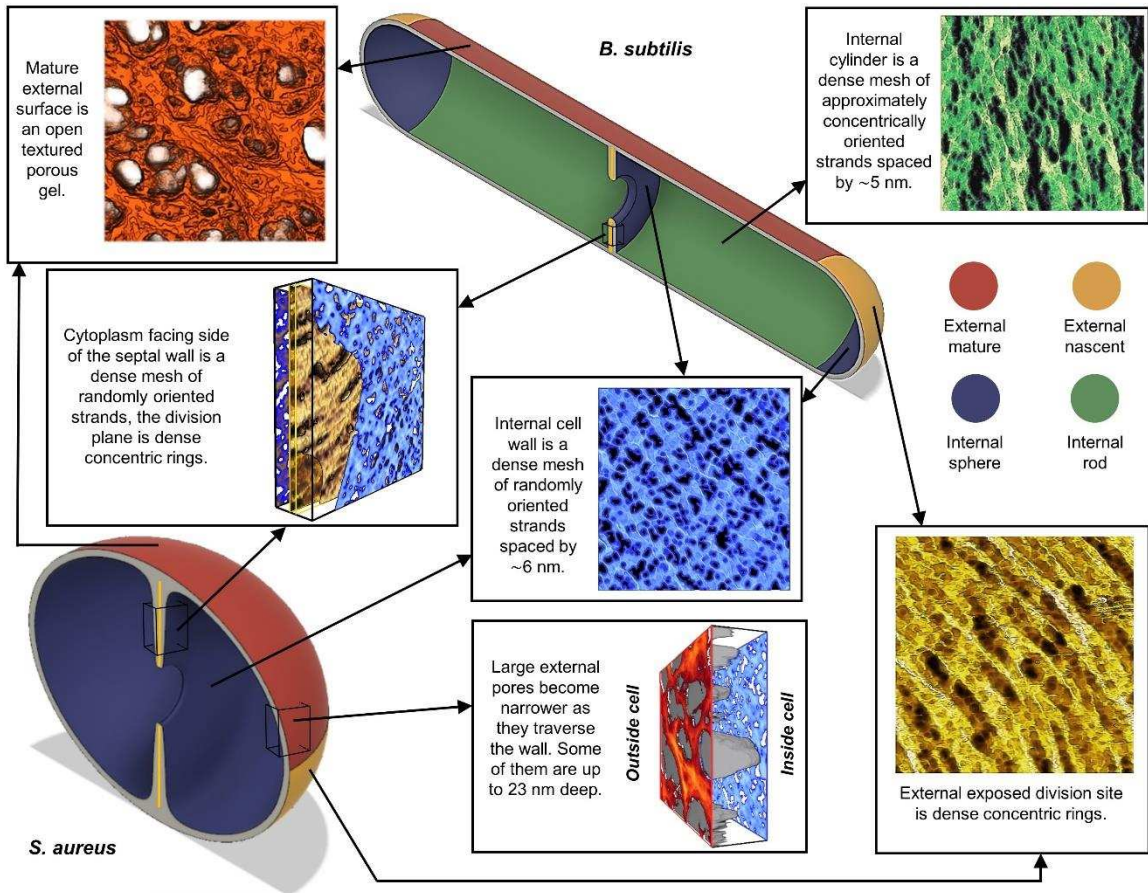


ED Figure 8

B. subtilis sacculi – partially-formed septa in different environments and different stages



ED Figure 9



ED Figure 10

**Supplementary information for:
The architecture of the Gram-positive bacterial cell wall**

L. Pasquina-Lemonche^{1,2,3y}, J. Burns^{1,2,3y}, R.D. Turner^{1,4,5}, S. Kumar^{1,2,6}, R. Tank^{1,2}, N. Mullin^{1,2}, J.S. Wilson^{1,4}, B. Chakrabarti², P.A. Bullough^{1,4}, S.J. Foster^{1,3,4*}, J.K. Hobbs^{1,2,3*}

¹ *Krebs Institute, University of Sheffield. S10 2TN. UK*

² *Dept. Physics and Astronomy, University of Sheffield. S3 7RH. UK*

³ *The Florey Institute, University of Sheffield. S10 2TN. UK*

⁴ *Dept. Molecular Biology and Biotechnology, University of Sheffield. S10 2TN. UK*

⁵ *Current address: Department of Computer Science, University of Sheffield. S1 4DP. UK*

⁶ *Current address: Dept. of Biochemistry, University of Oxford. OX1 3QU*

CONTENTS

Supplementary information 1: Video showing a tomogram of a purified frozen hydrated *S. aureus* sacculus.

Supplementary information 2: MATLAB code for obtaining peptidoglycan strand orientation.

Supplementary information 3: Estimation of the critical pore size to maintain plasma membrane integrity.

Supplementary information 1

Video showing a tomogram of a purified frozen hydrated *S. aureus* sacculus.

(Seconds 0 to 4) The video "Video_SI1.mp4" shows the tomogram from the bottom to the top. There is a first stopping point which corresponds to where image ED6b was extracted from and then a second stopping point corresponding to ED6a.

Each slice shown on the tomogram corresponds to 1.3 nm. Images ED6a-d correspond to 10 slices thick, which means they represent 13 nm of the tomogram.

(Seconds 4 to 7) Later on in the video, the slices are shown from top to bottom, with an isosurface (in green) manually drawn showing the outline of the sacculus.

Supplementary information 2

MATLAB code for determining glycan strand orientation

```
% read the image into MATLAB and convert it to grayscale

I = imread('image_name.jpg'); %enter name of file within ' '
Igray = rgb2gray(I);
figure, imshow(I);

% We will clean it up with a few morphological operations
Ibw = im2bw(Igray, graythresh(Igray));
se = strel('line',3,200);
cleanI = imdilate(~Ibw,se);
figure, imshow(cleanI);

% Perform a Hough Transform on the image The Hough Transform identifies
lines in an image
[H,theta,rho] = hough(cleanI);
P = houghpeaks(H,300,'threshold',ceil(0.5*max(H(:))))); %find peaks with a
threshold of minimum signal to be considered a peak

%the houghlines function defines how to draw the lines. Variable parameters
are: Fill Gap (defines minimum space between two lines). Min Length defines
the minimumsize of a marked line. The numbers were optimized using the set
of images available.
lines = houghlines(cleanI,theta,rho,P,'FillGap',3,'MinLength',15);

%Plot the lines on top of image marking the beginning and end
hold on
max_len = 0;
for k = 1:length(lines)
    xy = [lines(k).point1; lines(k).point2];
    plot(xy(:,1),xy(:,2),'LineWidth',2,'Color','green','LineStyle','-');

    % Determine the endpoints of the longest line segment
    len = norm(lines(k).point1 - lines(k).point2);
    if ( len > max_len)
        max_len = len;
        xy_long = xy;
    end
end
hold off

%To be able to plot the angles using the rose function, it is necessary to
transform all the degree values of theta to radians using deg2rad.
hold on
for k = 1:length(lines)
    lines(k).theta = - deg2rad(lines(k).theta);
end
hold off

%plotting the results (angles between 0-180)
figure;rose([lines.theta]);
```

MATLAB code used to automatically detect lines that were manually drawn on top of the images. The drawing had to follow certain rules for the program to work: it only detects straight lines, they must be of approximately similar length and width. A Windows laptop/tablet was used to draw on top of each image following these guidelines. Then, the Hough transformation creates a matrix where for each beginning and end of a line, it associates a vector to it and an orientation angle. The function 'rose' at the end of the code produces the rose diagrams representing the angle distribution of the vector lines. θ , it plots the different angles with respect to the reference being the vertical axis of the image set to 0 degrees. This process was repeated for all the images analysed without altering any parameter, to produce the angle distribution for each image.

Supplementary information 3

Estimation of the critical pore size to maintain plasma membrane integrity.

Our calculation is rooted in the elastic deformation energy of a membrane given by the Helfrich-Canham form¹,

$$F_H = \frac{\kappa}{2} \int H^2 dA, \quad \text{eqn. 1}$$

where κ is the bending modulus of the membrane, H , the mean curvature, and dA the surface area element. We note that the spontaneous curvature of the membrane is assumed to be zero. Since the Gaussian curvature integrates to a constant term via the Gauss-Bonnet theorem for closed membranes the elastic deformation term corresponding to Gaussian curvature is neglected in Eq. 1. We visualize the cell membrane as a closed continuous sheet without any holes.

The mean curvature, $H = \frac{1}{2}(c_1 + c_2)$ where c_1 and c_2 are the principal curvatures of the membrane. For a hemispherical bulge of radius R the Helfrich-Canham free energy is given by

$$F_H = \pi\kappa. \quad \text{eqn. 2}$$

The work done to cause the membrane to deform into a hemispherical bulge will be given by $P\Delta V$ where P here is the turgor pressure of the cell and ΔV is the volume associated with the bulge. This gives a critical pressure to form the hemispherical bulge of

$$P_{\text{crit}} = \frac{3\kappa}{2R^3}. \quad \text{eqn. 3}$$

At pressures above this we expect the membrane would start to escape out through the hole, ultimately leading to cell death. i.e. P_{crit} here is the maximum turgor pressure that the cell can sustain.

We calculate the expected maximum pore size for the expected cellular turgor pressure of approximately 20 bar. R is taken to be half the measured pore diameter. Values for the bending modulus of Gram positive cell membranes are hard to find in the literature. We estimate that κ is in the range 20-70 $k_B T$, the lower bound being the bending modulus for a lipid membrane, in line with Daly *et al*² and the upper bound being the bending modulus for a eukaryotic cell membrane lacking anchoring to the actin cortex³. For a turgor pressure of 20 bar, this gives us an estimated critical pore diameter of 8-12 nm, implying that the pores seen are just small enough that membrane rigidity is able to maintain cell turgor.

References

1. Helfrich, W. "Elastic Properties of Lipid Bilayers Theory and Possible Experiments", Z. Naturforsch. C 28 693-703 (1973)
2. Daly, E.K., Huang, K.C., Wingreen, N.S., Muckhopadhyay, R. "Mechanics of membrane bulging during cell-wall disruption in Gram-negative bacteria" Phys. Rev. E 83, 041922 (2011)
3. Simson, R., Wallraff, E., Faix, J., Niewöhner, J., Gerisch, G., Sackmann, E. "Membrane bending modulus and adhesion energy of wil-type and mutant cells of Dictyostelium lacking Talin or Cortexillins" Biophys. J. 74, 514-522 (1998)